SANDIA REPORT

SAND2015-4371
Unlimited Release
Printed June, 2015

Ductile Tearing of Thin Aluminum Plates Under Blast Loading: Predictions with Fully Coupled Models and Biaxial Material Response Characterization

Edmundo Corona, Arne S. Gullerud, Kimberly K. Haulenbeek and Phillip L. Reu

Prepared by
Sandia National Laboratories
Albuquerque, New Mexico 87185 and Livermore, California 94550

Sandia National Laboratories is a multi-program laboratory managed and operated by Sandia Corporation, a wholly owned subsidiary of Lockheed Martin Corporation, for the U.S. Department of Energy's National Nuclear Security Administration under contract DE-AC04-94AL85000.

Sandia National Laboratories

Issued by Sandia National Laboratories, operated for the United States Department of Energy by Sandia Corporation.

Available to DOE and DOE contractors from
U.S. Department of Energy
Office of Scientific and Technical Information
P.O. Box 62
Oak Ridge, TN 37831

Telephone: (865) 576-8401
Facsimile: (865) 576-5728
E-Mail: reports@adonis.osti.gov
Online ordering: http://www.osti.gov/bridge

Available to the public from
U.S. Department of Commerce
National Technical Information Service
5285 Port Royal Rd
Springfield, VA 22161

Telephone: (800) 553-6847
Facsimile: (703) 605-6900
E-Mail: orders@ntis.fedworld.gov
Online ordering: http://www.ntis.gov/help/ordermethods.asp?loc=7-4-0#online

SAND2015-4371
Unlimited Release
Printed June, 2015

Ductile Tearing of Thin Aluminum Plates Under Blast Loading: Predictions with Fully Coupled Models and Biaxial Material Response Characterization

Edmundo Corona, Arne S. Gullerud, Kimberly K. Haulenbeek
and Phillip L. Reu

Abstract

The work presented in this report concerns the response and failure of thin 2024-T3 aluminum alloy circular plates to a blast load produced by the detonation of a nearby spherical charge. The plates were fully clamped around the circumference and the explosive charge was located centrally with respect to the plate. The principal objective was to conduct a numerical model validation study by comparing the results of predictions to experimental measurements of plate deformation and failure for charges with masses in the vicinity of the threshold between no tearing and tearing of the plates. Stereo digital image correlation data was acquired for all tests to measure the deflection and strains in the plates. The size of the virtual strain gage in the measurements, however, was relatively large, so the strain measurements have to be interpreted accordingly as lower bounds of the actual strains in the plate and of the severity of the strain gradients. A fully coupled interaction model between the blast and the deflection of the structure was considered. The results of the validation exercise indicated that the model predicted the deflection of the plates reasonably accurately as well as the distribution of strain on the plate. The estimation of the threshold charge based on a critical value of equivalent plastic strain measured in a bulge test, however, was not accurate. This in spite of efforts to determine the failure strain of the aluminum sheet under biaxial stress conditions. Further work is needed to be able to predict plate tearing with some degree of confidence. Given the current technology, at least one test under the actual blast conditions where the plate tears is needed to calibrate the value of equivalent plastic strain when failure occurs in the numerical model. Once that has been determined, the question of the explosive mass value at the threshold could be addressed with more confidence.

Acknowledgment

We would like to acknowledge Eliot Fang for funding this project. The blast-on-plate experiments were initially conducted by Jerry Stofleth and Venner Saul, who also built the test facilities used. James Phelan, Kenneth Gwinn and Jeffrey Gruda coordinated the model validation for the one-way coupled model, with the latter and Jonathan Rath conducting a large portion of the computational work. Uniaxial tension testing of the plate material was carried out by Wei-Yang Lu. The biaxial material tests were conducted at the University of Texas at Austin by Prof. Stelios Kyriakides and John Mersch through a contract between SNL and UT-Austin. Felicia Pankratz kindly assisted us setting up and managing the contract. We would also like to acknowledge people who showed interest in the project and provided valuable technical insight. They include Stephen Attaway, Eugene Hertel of SNL and Steven Alves of LLNL. The latter conducted parallel validation work on the problem at hand using ParaDyn and ALE 3D. Finally we would like to acknowledge Benjamin Reedlunn, who reviewed this report and gave us extensive and pertinent commentary.

Contents

Appendix

Figures

Tables

Nomenclature

A, n	Power law fit coefficient and exponent
E	Modulus of elasticity
K	Pressure loading magnification factor
P	Pressure
P_{atm}	Standard atmospheric pressure
R	Plate radius
S	Standoff distance
e_1, e_2	Strain components in the bulge test of Kyriakides and Mersch (2013)
e_1^p, e_2^p, e_3^p	Plastic strain components in the bulge test of Kyriakides and Mersch (2013)
e_e^p	Equivalent plastic strain in Kyriakides and Mersch (2013)
m	Charge mass
r	Radial coordinate
t	Time
w	Out-of-plane deflection
Δ	Out-of-plane deflection at the center of the plate
ΔP	Additional pressure in Zapotec analysis
Δt	Time increment
δ	Distance in CTH vs Zapotec comparisons
ε_e^p	Equivalent plastic strain
ε_{eo}^p	Equivalent plastic strain at failure
$\varepsilon_{rr}, \varepsilon_{\theta\theta}$	Radial and circumferential strain components
ν	Poisson's ratio
ρ	Explosive density
σ_1, σ_2	Stress components in the bulge test of Kyriakides and Mersch (2013)
σ_o	Yield stress
σ_e	Equivalent (von Mises) stress

1 Introduction

Many problems of interest at Sandia involve the response and failure of structures subjected to detonation-driven blast loads. Numerical simulations of this kind of problems are one of the principal tools used to attempt predictions of the behavior and failure of the structures. The problems, however, are generally very complex because they involve modeling of the detonation, of the structural response and of the coupling between the two. Each part is difficult in its own right and involves significant nonlinearities. It is therefore imperative to conduct validation studies to assess the performance of numerical models against experimental data. Without them, very little confidence can be placed on the results of simulations. The objective of the work presented here is to conduct a validation exercise of simulations of blast of a C4 charge in air and in close proximity to a thin aluminum circular plate. Comparison between the model predictions of plate deflection and tearing against experimental measurements and observations represents the main measure for validation.

The type of problem addressed here is generally posed as follows: Given an explosive type, its mass, shape and location with respect to a structure, determine the response of the structure and whether it will fail and how. Of course, it is assumed that the geometry of the problem, the properties of models for the explosive and the surrounding environment as well as the material properties of all structural components have been determined. Further information such as the type of detonator used and its location within the explosive mass may in some cases also be needed to properly represent the characteristics of the blast.

Scientific work on the topic of the response of blast loaded plates has been conducted at least since the second half of the 19th century. The earliest work located during a review of the literature is that by Adamson (1878), who subjected iron and steel plates to detonations of guncotton (nitrocellulose). His work was motivated by situations where a boiler could be impacted by the explosion of a neighboring unit. The blasts were strong enough to cause failure, and he concluded that mild steel plates were superior to cast iron ones, but that a proper composition of the steel alloy was of high importance to increase plate resistance to failure. Other early investigations mentioned in the literature were motivated by the response of ship hulls to underwater explosions and conducted by the Imperial Japanese Navy in 1924 (Rajendran and Narasimhan, 2001). G.I. Taylor (1941) also addressed the topic of underwater blasts impinging on plates during the period of WWII in an often-cited article. The emphasis of that paper was to study the effect of the motion of the plates on the magnitude of the reflected pressure. The application of blast loads on plates also has applications in thin sheet forming (Kalpakjian,1995) as well as in other manufacturing processes as indicated in the book by Blazynski (1983).

The variety of configurations in which structures and blast loads can interact is quite extensive. For example, blasts can originate from spherical charges, sheet explosives, or explosives with other shapes. The type of explosive can also vary greatly. The variety of targets can also be bewildering, even if restricted to plates. The plates can be made of various metal alloys that are of monolithic or composite construction (sandwich plates, for example) or can also be non-metallic (plastic, fiber reinforced composite, etc.). They can vary in

their in-plane dimensions and have a range of thicknesses; plus they can be monocoque or reinforced by stiffening members. Many explosive/plate arrangements are also possible. For example: underwater or air detonations where the explosive is positioned at some standoff distance from the plate, or where the explosive and the plate are in contact, or perhaps where another material is between the explosive and the target. In some cases just the response of the plate is of interest whereas in others failure is also important. Clearly the breadth of the field is immense. A rather modest review of the literature was conducted with the objective of establishing what work has been conducted since the middle of the 20th century on the topic of blast on metal plates and therefore give some perspective to the work presented in this report. The emphasis will be on blast loaded plates where the loading comes from an explosive charge in air at atmospheric pressure. As expected, the literature contains references to several other blast-plate interaction configurations, both experimentally as well as analytically. For example, experiments on plates pre-loaded by a pressure differential of 0.4 atmospheres were conducted by Veldman et al (2006 and 2008). They found that the pressure differential had very little effect on plate deflections but a large effect on the extent of damage when the plates failed. Langdon and Schleyer (2003) used a "fast differential pressure device" to apply better controlled dynamic pressure histories to plates than can be obtained with explosive charges. Underwater blasts have also been considered, see (Rajendran and Narasimhan, 2001) and (Ramajeyathilagam et al, 2000) as well as a sort of inverted problem where the underwater collapse of a cylindrical shells generates a pressure shock that could impinge on nearby structures (Farhat, 2013) .

A lot of the work conducted has been experimental. Indeed, experimentation has been a constant in this topic, and the reason is simple. Both the detonation and the plate response are very complex processes that are difficult to accurately model mathematically on their own, let alone trying to also model their interaction. This complexity has precluded the use of analytical models and created significant challenges to more modern computer simulations. Therefore, experimental studies have been paramount to establishing the actual response and failure of blast loaded plates.

Early work was concerned with the circular geometry. Nurick and Martin (1989b) reported on a survey of experiential studies conducted prior to their publication . This paper was accompanied by a sister survey on theoretical considerations (Nurick and Martin, 1989a) that concentrated on calculations of the final deflection of plates. The works cited are in general analytical in nature and include significant simplifying assumptions. Examples of early theoretical work include the work of Hudson (1951), who derived a model for the motion of circular elastic-plastic plates based on experimental observations of the shape of the plates. He took the effect of the blast to be an initially uniform initial velocity over the entire plate. Similar boundary conditions were considered by Wang and Hopkins (1954) using a more theoretical approach. Florence (1966) considered the application of a constant pressure over a prescribed circular region and applied for a given time period to construct an analytical model that described the initial deformed shape of the plates. As in most other analytical works, a rigid-plastic material model with a Tresca yield surface was used. Krajcinovic (1972a and 1972b) also developed models under similar assumptions in a two paper series. In the first, he considered a uniformly distributed load with arbitrary time

history, while in the second he considered a centrally loaded plate with a uniform spatial magnitude but arbitrary time history.

Whereas a lot of the analyses in the 1960's and 1970's involved the use of simplified models, a few investigators started considering the use of numerical techniques to address problems involving the dynamic deformations of thin-walled structural members. Witmer et al (1963) used a finite difference approach with lumped masses to discretize the equations of motion for thin-walled shells of revolution and assumed a von-Mises yield function with bilinear stress-strain response. They claimed reasonable agreement with experimental results for impulsive loading of various structures, including the final shape of circular plates circumferentially supported between knife edges under blast loading from a spherical charge. The experiments on flat plates that they used for comparison were conducted by Hoffman (1955) at the University of Delaware. The loading on the plate was taken to be either a uniformly applied impulse or a time history of uniform loading. The magnitude of the applied load was determined based on an experimentally derived smooth curve of explosive reflected impulses quoted by Hoffman[1].

Duffey (1967) conducted a series of experiments on impulsively loaded plates at Sandia National Laboratories. In these experiments, Al 6061-T6 and steel 1022 circular plates with diameter of 6 inches and thickness of either 1/16 or 1/8 inches were subjected to impulsive loads generated by a sheet of explosive with diameter of 2 inches and separated from the plate by a sheet of polyethylene 1/8 inches in thickness. The plates were clamped around their periphery. The study concentrated on measuring the dynamic deflection of the plates as a function of time using high speed streaking and framing cameras. The objectives of the study were to generate reliable data that could be used to assess the fidelity of deflection calculations by numerical methods and to assess whether uniaxial stress-strain curves of the material provided enough data to reasonably represent the material behavior. Comparisons of numerical simulations based on the work of Witmer et al (1963) to the experimental data are the subject of the report by Duffey and Key (1968). They reported reasonable agreement between the predictions and measurements of plate deflection.

Many contributions in the literature on the topic of plates subjected to blast loading have been conducted by G.N. Nurick and co-workers at the University of Cape Town in South Africa starting in the late 1980s. Two survey studies by Nurick and Martin (1989a and 1989b) have already been mentioned. Other works contain a combination of experiments and numerical analysis. The experimental arrangement favored by Nurick and co-workers consists of using sheet explosives placed over a polystyrene pad which in turn lies on the surface of the plate being tested; a similar stacking to that of Duffey (1967). The clamped plates are then placed over the open end of a hollow catch box mounted on a ballistic pendulum. This approach is also similar to that used by Bodner and Symonds (1979) who also recognized the intrinsic difficulty in restraining the in-plane motion of the plates under the clamping fixtures (this was also noted by Duffey and Key). Using this approach, Teeling-Smith and Nurick

[1]Hoffman refers to the work of Shirley Mills, "Measurements of pressures and impulses associated with blast waves," Masters thesis submitted to the Johns-Hopkins Univ., March 1955. This work has not been consulted.

(1991) studied the deflection and failure of circular cold-rolled mild steel circular plates when the diameter of the explosive/pad combination was apparently equal to the plate diameter. In these cases, failure occurred at the support of the thin plates (diameter-to-thickness ratio seems to be 63). The mode of fracture changed from a tensile mode to a shear mode as the strength of the blast increased. Subsequent work by Nurick et al (1996) on circular plates was extended to investigating the effect of whether the edge of the clamping fixtures was sharp or smooth with a radius. They found that the plates tested with the smooth radius clamp deflected further prior to failure. This paper also includes finite element analysis in Abaqus to study the deformation at the boundary using axisymmetric continuum elements and a uniformly distributed pressure with a square function of time to match the impulses measured in the experiments. The numerical results had some discrepancies when compared to experiments, which the authors attributed to the material model. Later papers considered an experimental study of thin square plates (Nurick and Shave, 1996) and circular plates where the diameter of the sheet explosive was a fraction of the plate diameter (Wierzbicki and Nurick,1996). Although the main objective of the latter was to develop an analytical model for the motion of the plate, an interesting observation was that failure moved away from the edges and towards the center of the plates (disking) for localized charges of sufficient strength. The authors also acknowledged that the assumption that the impulse distribution is uniform over the diameter of the explosive and zero outside of it is too simplistic and that more complex distributions are required to improve the agreement of the final plate shapes between experiment and analysis. Rectangular plates subjected to localized blast loads were addressed by Jacob et al (2004). Similar observations regarding disking under the localized charges were made. This publication also reported on finite element numerical predictions using continuum elements in Abaqus. A relatively simple pressure profile based on the diameter of the explosive sheet, the burn speed and the measured impulses was applied to the plates in order to calculate their central deflection. Good agreement with experiments was reported. In a later paper by the group at the University of Cape Town (Jacob et al, 2007), they considered a different set-up for applying the blast loading to the plates: detonating a charge at one end of a steel tube, with the plate located at the other end. Their objective was to study the effect of stand-off distance on the central deflection of the plates. In their review of previous work, they indicate that a petaling mode of failure had also been observed for very high impulses applied in a localized manner. Their results showed that center deflections decrease with increasing standoff distance, but become insensitive to standoff as it becomes large.

Early attempts at numerical predictions of plate behavior conducted in the 1960s and 70s were mentioned previously. As can be expected, those efforts did not have the capabilities regarding the discretization of the problem, simulation of actual blast loads and modeling of material failure that characterize modern analyses. By the late 1990s, attempts started being reported of finite element analyses that include failure criteria as in the work of Rudrapatna et al (1999) although the pressure loading was still assumed to be uniformly distributed over the plate and to be a square pulse with respect to time. A similar analysis of the experiments by Teeling-Smith and Nurick(1991) and Nurick et al (1996) was conducted by Gupta and Nagesh (2007) and reported good agreement with experiment. Neuberger et al (2007) conducted both experiments and analysis of the deflection of circular plates

subjected to blast from a nearby spherical charge in order to assess a scaling procedure to transfer scaled-down tests to larger full-scale scenarios.

More sophisticated models were reported by Balden and Nurick (2005). Here they simulated the experiments by Teeling-Smith and Nurick (1991) using Abaqus/Explicit with continuum elements and included a plastic strain failure criterion. They gathered their material parameters from several sources and implemented them in a model that included strain-rate dependence and temperature. The plastic strain at failure was taken to be 200%, but the origin of this number was not clear. They also considered another example where the blast load was localized with respect to the dimensions of the plate. Here they employed the Johnson-Cook strength and failure material models. The parameters of the model were selected from values available in the literature for mild steel. Another important advance presented in this paper was the use of hydro-dynamic codes (AUTODYN-2D) to obtain pressure histories to be applied to the plate based on the simulation of the blast using the Jones-Wilkins-Lee (JWL) equation of state (Lee et al, 1968) for the explosive. The harvested pressures provided pressure-time histories on the surface of the plate. Based on the envelope of the peak pressures at all radial locations from the center of the plate, a pressure-radial distance function was constructed and applied to the finite element model of the plate for the duration of the burn time. Using this model they found good agreement between analysis and experiment for the center deflection of the plate. The predictions of localized thinning and failure are at least qualitatively correct. A later work by Safari et al (2011) also considered the use of the JWL equation of state within AUTODYN to calculate rectangular plate deflections using what appears to be fully coupled calculations. Alves et al (2012a) conducted calculations of the deflection and failure of the same plates addressed in this report by mapping pressures calculated using the hydrodynamic code ALE3D onto a ParaDyn model. They found that the predictions by the JWL model underestimated the deflection of the plates, which led them to develop an enhancement (Alves et al, 2012b) that will be discussed later in this report. They used the Johnson-Cook model with properties adapted from the literature and uniaxial tension tests to represent the material deformation and failure. They reported good agreement with experiments.

Due to the very fast deformation of plates subjected to blast loads, it has been difficult to make measurements of plate deformation as a function of time. With the exception of the work by Duffey (1967) only the final deformation of the plates are reported for all work conducted prior to the mid-2000s. The final deformation has also been the principal method to compare the results of analysis against experimental data. This issue has been significantly alleviated by the development of high-speed stereo digital image correlation (DIC) techniques. Stereo DIC has the capability to provide three-dimensional full-field measurements of plate deformation as demonstrated by Tiwari et al (2009) for plates subjected to blast by buried charges. In the present work, significant use has been made of high-speed stereo DIC to calculate deformation measures of the plates considered. The technique and results will be discussed in detail.

The motivation for the current work originated from a previous validation effort on the same problem that utilized a simpler approach where the blast and the structural response

were calculated in separate analyses. In this uncoupled model, the pressure-time histories generated by the blast model are first harvested on a representation of a rigid plate. In the subsequent finite element analysis of the plate structural response, the harvested pressures are applied to the surface of the plate model. The particulars of this approach and of the predicted results will be considered in more detail in Section 4. For the purposes of this section, however, it suffices to state that although plate deflections were reasonably accurately calculated with this approach, plate failure was not predicted well, even in a qualitative manner. In essence, the prediction of the location of first tearing in the plate was wrong.

The objective of the present work was then to utilize a more sophisticated blast-on-plate model that included full coupling between blast and structural response. A fully coupled model is one where the blast and the structural response are calculated simultaneously. In other words, the pressure wave generated by the blast causes motion of the structure which in turn affects the pressures on the plate surface. In addition, the model also included the motion of the air that surrounds the explosive and the plate. Therefore, the coupled model is the most representative tool that can be used to study the problem at hand. The present work was conducted to see if use of the coupled model resulted in better predictions of the location of first failure in the plates while still producing reasonable predictions of the plate deflections.

The rest of the report is organized as follows: Section 2 describes the experimental set-up, including the geometry of the plate and the location of the explosive mass, the high-speed stereo digital image correlation (DIC) techniques used to measure deflections and strains, and the results obtained of plate deformation and failure. Results obtained to date on the characterization of the plate material up to failure follow in Section 3. Section 4 presents a summary of the uncoupled model approach that was used prior to the present work and a sample of the results obtained. This is followed by a description and presentation of the results of the fully coupled model that was at the heart of the present approach in Section 5. Section 6 presents a more detailed analysis of the structural predictions by the fully coupled model and comparisons with the experimental results in light of the latest material characterization activities. Finally, Section 7 presents a summary of the work conducted, conclusions and recommendations for future work.

2 Experiments

2.1 Experimental Set-up

All plate blast experiments were conducted at the 9930 explosives facility at Sandia National Laboratories-New Mexico. Figures 1(a) and (b) show different views of the test fixture while Fig. 2 shows schematics of two planes of the experimental set-up. The test fixture's principal component was a 2 in. (5 mm) thick, square steel plate with a 44 in. (1.12 m) diameter hole cut in the center. The plate rested on two I-beams which were supported by a concrete platform as can be seen in Fig. 1. The aluminum plate specimen had a diameter of 48 in. (1.22 m) and was installed over the hole of the steel plate and clamped using a steel ring with a 2×2 in. (5×5 cm) square cross-section. Clamping was accomplished by using 45 5/8-UNF Grade 8 bolts torqued to 250 ft-lb (340 N-m) as illustrated in Fig. 2. No slippage was observed to have occurred at the aluminum plate boundary during the tests. The material in all specimens was Al 2024-T3. Most of the relevant results of this study were obtained using specimens with thickness of 0.040 in. (1.02 mm), giving a radius-to-thickness ratio (R/t) of 550. A few specimens with thickness of 0.063 in. (1.60 mm) or $R/t = 350$ were also tested and are included in this work to illustrate the effect of thickness on the response of the specimens.

The specimens were painted with a speckle pattern on the side opposite to the blast in order to enable displacement measurement using 3D digital image correlation (DIC) as shown in Fig. 1. The test fixture was also painted with a speckle pattern in order to correct for any displacement of the structure in which the plates were mounted. The deflection of the fixture, however, was found to be negligible. The motion of the specimen was recorded using two high-speed video cameras operating at 36,000 frames per second. The cameras were located approximately 20 ft (6 m) from the center of the plate approximately 9 ft (2.7 m) apart with an included angle of about 25° as illustrated in Fig. 2. The software used for digital image correlation was Vic3D produced by Correlated Solutions, Inc. In addition to the two high-speed video cameras used for 3D digital image correlation, a Phantom high speed video camera was used in some tests to capture a side view of the event at 12,500 frames per second. Further information regarding the DIC setup and analysis will be given in Section 2.2.

In all tests, the blast loads were generated by charges of C4 explosive formed into spheres and center-initiated with RISI (Reynolds Industries Systems Inc.) RP-83 bridgewire detonators. The detonators consist of a cylindrical aluminum shell with diameter, thickness and length of 0.28, 0.007 and 1.56 inches (7.1, 0.18, 39.8 mm) respectively that contain an 80 mg (0.0002 lb) PETN initiating charge within a copper sleeve and 1.031 g (0.0023 lb) of RDX with binder as an output explosive. The C4 charges used on plates with thickness of 0.063 in. were hand-formed, while the charges made for the plates with thickness of 0.040 in. were formed using molds to make the geometry and density of the charges more consistent. Since C4 holds its shape after forming, these charges were bare when detonated. Each charge had a density of 1.60 ± 0.02 g/cc (0.0578 ± 0.0007 lb/in^3). In order to minimize the possibility

of detonator fragments hitting the plates, the detonators were oriented so the cylinder axis was oriented at 45° with respect to the normal of the specimen surface. For consistency, the axis of the detonator was also oriented towards one of the corners of the steel plate in the fixture. The high-speed videos of all tests were inspected for evidence of fragment impact, and those tests in which it was detected and led to premature failure were eliminated from consideration, as will be noted later. All the C4 explosive used in this study came from Accurate Energetic Systems, LLC (Lot # AGS08H032-018, Batch # 08AU08A1) and was kneaded prior to forming. In all tests the standoff distance between the center of the charge and the center of the plate was $S = 10$ in. (0.254 m).

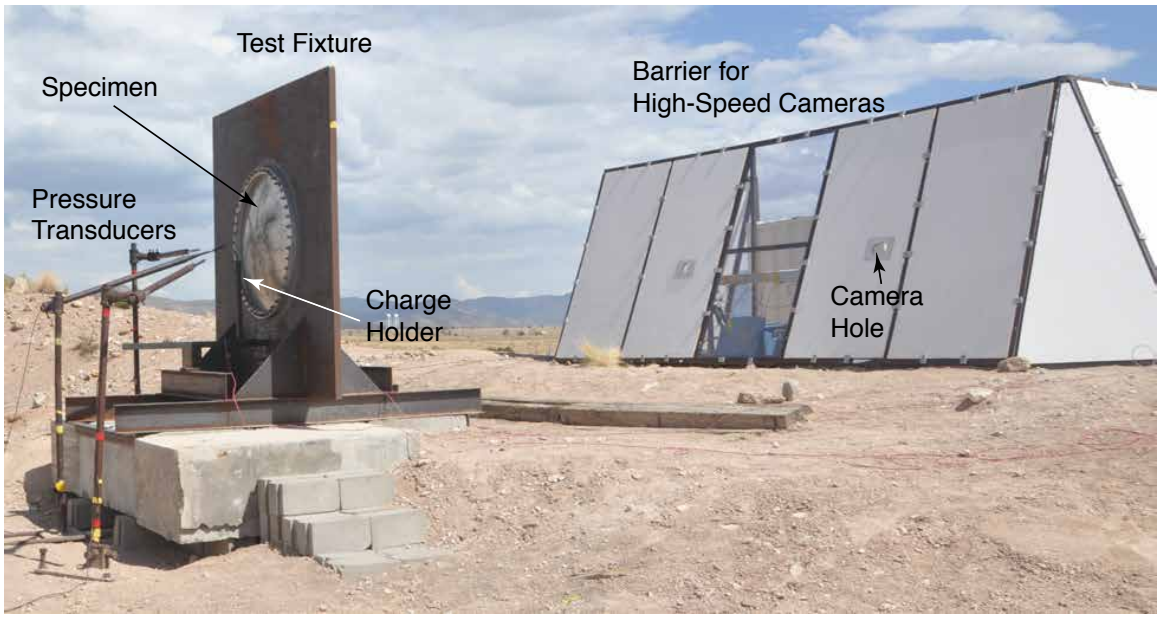

(a)

(b)

Figure 1. Photographs of the experimental set up. (a) Overall view of the test site showing the test fixture and the enclosure for the high-speed cameras and (b) view of the test fixture from the opposite side showing the speckle paint on the plate and on the fixture.

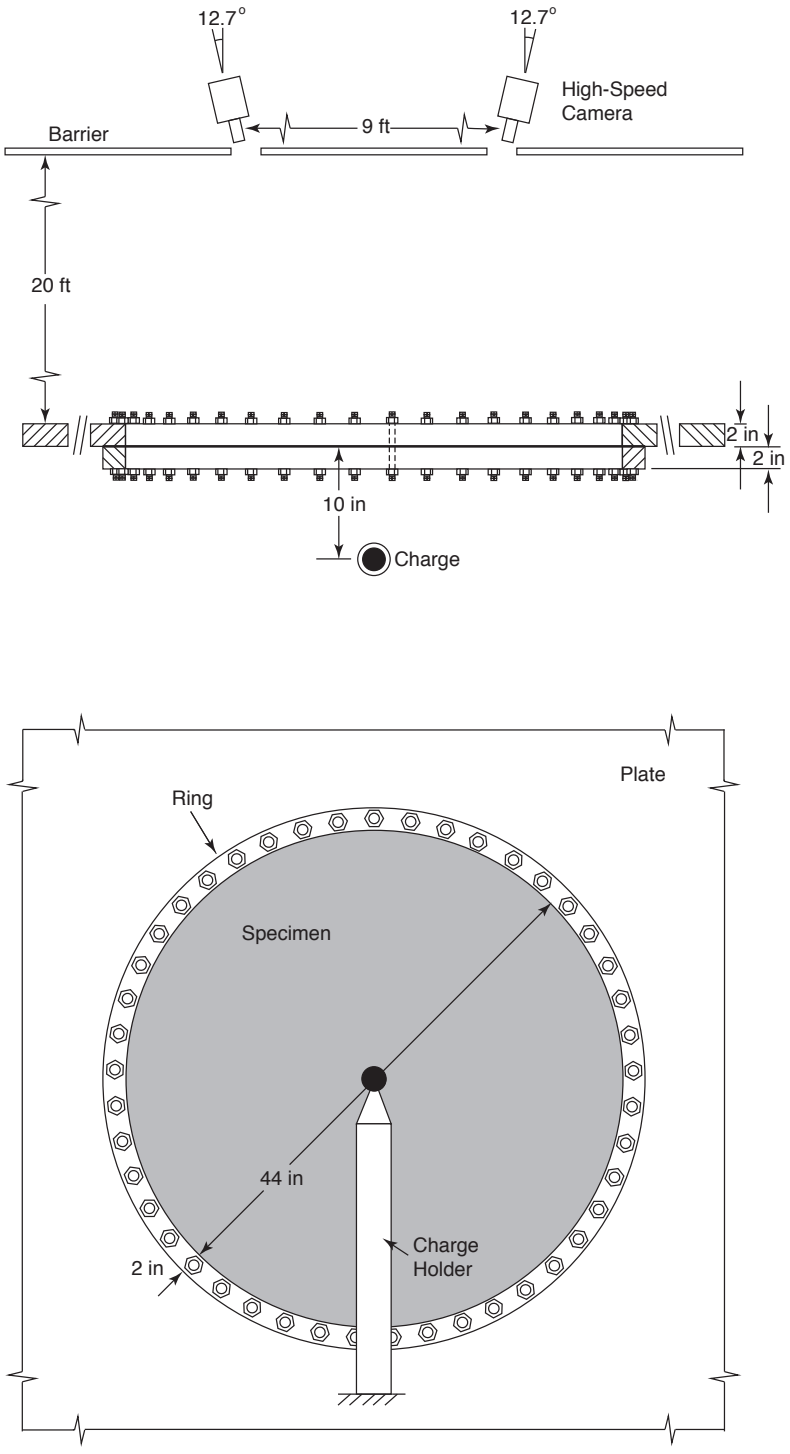

Figure 2. Schematics of two views of the experimental set-up.

2.2 Stereo-DIC Analysis

Three-dimensional digital image correlation (DIC) is a full-field optical technique that can measure the three-dimensional shape, position and deformation of surfaces. To make the measurements, a stereo-pair of cameras is first calibrated using a nonlinear optimization process or bundle-adjustment approach to determine the system's intrinsic and extrinsic calibration parameters. A high contrast speckle pattern applied to the surface can then be used to match pixel locations in the left image to the right image (cross-correlation) and also between the unloaded reference frame and following deformed frames (temporal correlation) for the stereo-cameras. The matching is done using a small square region of pixels called a subset. The cross-correlated subsets can then be triangulated using the camera calibration parameters. The details of DIC are well described by Sutton et al (2009). The technique allows thousands of data points to be measured at every time step with sub-pixel precision. The 3D position of each subset is the fundamental measurement, with displacement calculated by subtracting the 3D position of the reference frame from any deformed frame. Using the displacement data, it is then possible to use a number of data points to calculate the displacement gradient to determine strain. The following sections detail the experimental setup and analysis process for this test series.

DIC Experimental Setup

Two synchronized Vision Research Corp v12 high-speed cameras fitted with Nikon 28-85 mm zoom lenses were used to acquire images as a stereo-pairs. The frame rate was 36,000 frames per second. Each frame had 384×376 pixels and spatial resolution of 0.22 in/pixel (5.5 mm/pixel). The field of view was optimized to contain the entire specimen and a small surrounding area of the thick mounting plate. The mounting plate was also speckled to allow measurement of its motion due to the pressure loading of the blast. Its motion was less than 0.04 in. (1 mm) during the first 2 ms after detonation, which is the time range of interest in this work, and less than 0.140 in. (3.5 mm) after 5 ms. Contrast this to the maximum deflection of the specimen, which at 2 ms was in the order of 4.4 in. (110 mm) for the smallest charge mass considered. The motion of the mounting plate was therefore neglected for all of the subsequent analysis. The cameras and the explosive were triggered simultaneously. A few pre-trigger frames were also kept to capture the static shape of the plate before loading. The cameras were positioned behind a plywood barrier to provide some protection from flying debris. No protection was used right in front of the cameras during testing to avoid optical distortions by transparent protecting materials. The cameras were also mounted with stiff plates on a single stiff beam to provide pan adjustment and minimize camera motion and loss of calibration. Since the set-up was located outdoors, shadows were a problem in early testing; therefore, a shade was implemented to provide flat lighting without shadows. This setup is shown in Fig. 3 (a) while Fig. 3 (b) shows the location of the cameras behind the plywood barrier. A time fiducial seen by the cameras was also included that consisted of a flash synchronized with the initiation of the explosive to determine the frame at zero time (detonation time) from the high speed video images.

(a) (b)

Figure 3. Optimized DIC setup. (a) Shade structure to provide flat illumination and plywood shielding for the cameras with view ports and (b) unified single mounting stiff beam for the cameras.

Each sample was prepared for measurement by first cleaning the surface with a degreaser and then painting it flat white with auto paint. After drying, a stencil pattern was used to create a contrasting pattern using black paint. The speckles were sized to be approximately 4 pixels when imaged by the cameras. This optimized speckle size allowed the highest spatial resolution, without aliasing of the speckles, which would degrade in the results. For the high-strain rate testing of this test series, it was important that the paint be applied within 1 to 2 days of the test. If the paint was allowed to age longer, de-bonding of the paint during the experiment was likely.

Spatial Resolution of the DIC Measurements

The spatial resolution of the displacement measurements is fundamentally determined by the subset size and step size used in the DIC analysis. The subset defines the region of the image that is used for correlation and the step size defines the distance between subset solutions. Subset sizes of approximately 17×17 pixels were used, which was sufficient to contain enough speckles to yield accurate correlation without being too large for the underlying displacement field. Figure 4 shows a grid of 17×17 pixel subsets and their size relative to the speckle pattern.

The first objective of the DIC measurements was to first provide Cartesian data sets of the displacements and strains in the specimens. A step size of three pixels was used, giving a displacement measurement every 0.65 in. (16.5 mm). The 3-pixel step size creates a condition with some dependence between solutions and therefore some correlated noise between data points. However, Gaussian subset weighting somewhat mitigated this by assigning less weight to the pixels near the edges of the subsets. A larger step size is not desired in this situation

due to the decrease in number of data points spatially. The second objective was to use the Cartesian data set to determine displacement and strain profiles in order to obtain the mean profiles of displacement and strain assuming axisymmetric conditions. These will be described in more detail later in this section.

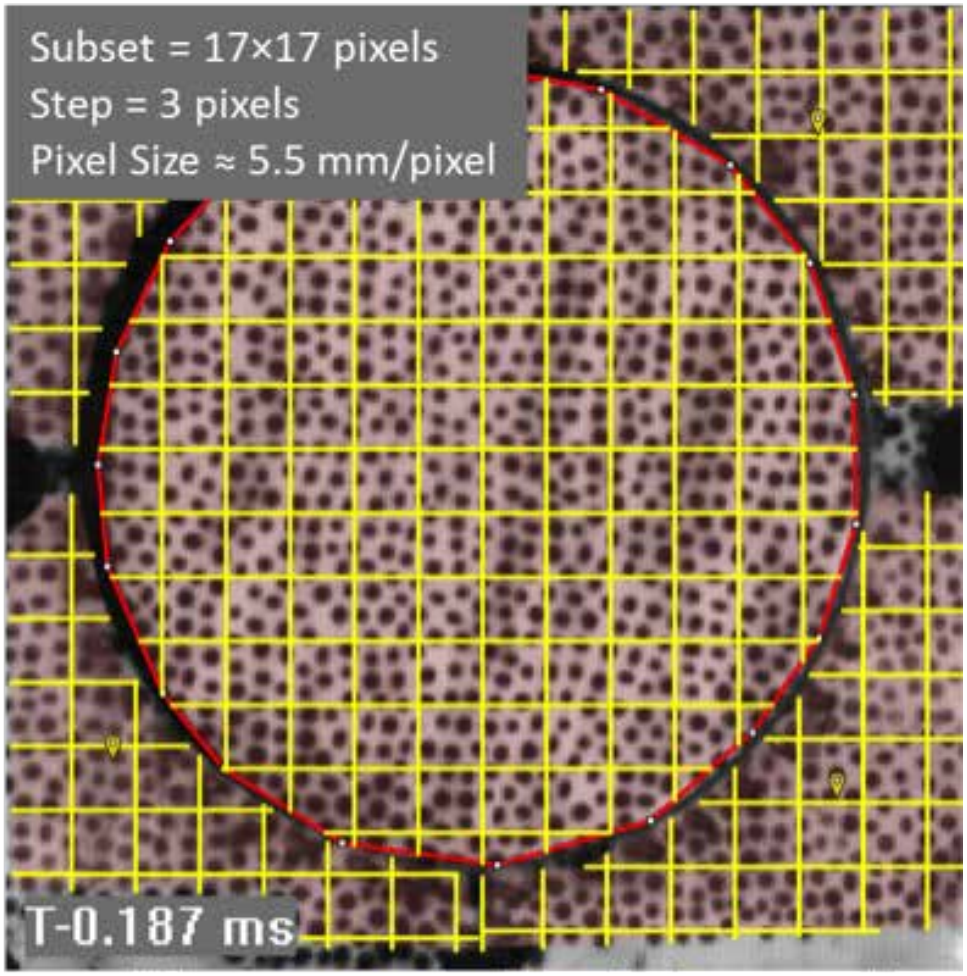

Figure 4. Illustration of subset and region-of-interest (ROI) for DIC analysis, with a grid of 17-pixel subsets and 17 pixel step size. The actual step size in most measurements was 3 pixels, giving more closely spaced displacement measurements than shown. Wavy appearance of the plate surface is an illusion from the painted pattern.

A standard measure of the uncertainty is the noise floor measurement. This measurement is done by taking 6 frames immediately before detonation, and then averaging the standard deviation of each of the three displacement components. This gives an indication of the matching noise and the resultant errors in the displacement measurements. The average noise floor measurements errors from seven tests were in the order of 0.08×10^{-3} in. (0.02

mm) for the in-plane displacement components and 3.5×10^{-3} in. (0.09 mm) for the out-of-plane component. Both are well below the actual values induced by the detonation. For example, for the smallest charge mass considered, 120 g, the maximum in-plane and out-of-plane displacements were 0.24 in. (6 mm) and 4.4 in. (110 mm).

Lagrangian strain calculations were carried out using the Vic3D software[2]. The calculations involved discretizing the deformed surface into triangles with vertices at the points where the position of the plate had been determined. Assuming the strain in the triangles was constant, the strains from four neighboring triangles that share one vertex were averaged to calculate the strain at that point. A second averaging followed over a square array of measurement points, called the strain window, using a Gaussian filter. In this work, the strain window was a set of 5×5 displacement data points. It yielded an apparent virtual gage size of approximately 13 pixels or 2.86 in. (73 mm). Remember that, however, 5 displacement measurements in a row actually corresponded to $17 + 4 * 3 = 29$ pixels on the images, which gave an area of influence of 6.4×6.4 in^2 (163×163 mm^2) for the strain calculation. The virtual gage size was relatively large and resulted in some filtering of the results that precluded truly local measurements in regions with sufficiently high strain gradients. A strain window of 5×5 displacement data points, however, was the smallest that the DIC software would allow in the calculations. Further decrease of the virtual gage length would have to be done separately by choosing fewer displacement points, but obviously limits exist as to how small the gage length can be with the data available. Furthermore, the measurement noise could also have increased significantly when trying to reduce the virtual gage length. Examples of strain calculations using two virtual gage lengths are shown in Appendix A.

Coordinate Transformation

The circular geometry of the specimens and the ideally axisymmetric loading caused by the detonation makes visualization of the results clearer in cylindrical coordinates than in the rectangular system used in data reduction. After determining the location of the center of the specimen, the transformation of coordinates, displacement components and strain components were carried out using standard formulas.

Axisymmetric Data Processing

Near axisymmetry of the specimen deflections was maintained in all tests for times below 1.25 ms after detonation or up to the time when tearing occurred, whichever came first. For plates that did not fail, wrinkling of the plate, which will be discussed in the next section, destroyed axisymmetry soon after the 1.25 ms time mark. To determine average axisymmetric profiles of the displacement and strain components of interest, each quantity was first determined at 50 evenly spaced rings around the plate, with 360 points around the circumference of

[2]Correlated Solutions produced a Vic-3D Testing Guide where the strain calculation is explained. It is not listed in the references because no publication date was given.

each ring. The values at each point in the rings were obtained by interpolating between measurements of the Cartesian data points. For every load step, the mean values and standard deviations of the quantities of interest were calculated within each ring. The standard deviation is a useful metric that indicates a combination of the measurement noise and/or any lack of symmetry in the response. For times prior to specimen failure or 1.25 ms, where there is a high degree of symmetry, the deviation is mostly an indicator of the measurement noise and lack of sphericity of the detonation. For later times, wrinkling of the plate can increase the value of the standard deviation. Sample results showing the magnitude of the standard deviation are shown in Appendix A.

2.3 Experimental Results

Pressure History

Before addressing the experimentally observed response of the plates it is instructive to have an idea of the nature of the pressure distribution on the plates in both space and time. Such measurements were not within the scope of the experiments, so the results of a numerical simulation will be considered instead. The calculations in the example to be discussed were conducted using the hydrodynamic code CTH (Crawford et al, 2013) to simulate the detonation of a 120 g sphere of C4 10 inches in front of a rigid surface simulated via a plane of symmetry. The model will be discussed further in Section 4, where a schematic is shown in Fig. 24 (a). The model was axisymmetric and accounted for the clamping ring mentioned in the previous section. In the case of the thin plates discussed in this work, the plates deflect in response to the pressure, and therefore the magnitudes and the details of the pressure distributions are different from those calculated. The principal aspects of interest at this time, however, can still be discussed based on this idealized model.

Figure 5 shows the results of interest in this discussion in the form of pressure distributions as functions of radial coordinate r, normalized by the plate radius R, and time t. The figure contains plots that represent the axisymmetric pressure distribution on the plate calculated at 44 locations. The CTH mesh was finer than that and therefore the reader must be warned that the frequencies of the fluctuations shown are aliases. In this discussion, however, only the low-frequency variations in pressure will be of interest. It takes just under 0.08 ms after detonation for the pressure front to reach the center of the plate. At this time, the pressure distribution affects only about 20% of the radius of the plate, as shown by the corresponding trace in the figure. Note that the pressures are relatively high, about 200 atmospheres. As time goes by, the pressure acts over a larger area, but the magnitude of the pressure decreases. Note that after 0.2 ms the pressure at the center has decreased considerably and the peak pressure is near the pressure front, which is now at a location 70% of the radius from the center. By 0.3 ms, the pressure front has reached the edge where the clamping ring is located. The interaction between the pressure and the ring causes a local increase in pressure at that location as shown by the trace at 0.4 ms. After another 0.1 millisecond, the local pressure near the ring has decreased considerably and extended to a distance about 20% of the radius from the edge. After 0.5 ms, the detonation pressure field essentially ceases to act on the plate at the scale shown in the figure. A small pressure rise occurred at $r = 0$ at about 0.8 ms, probably due to the convergence of the reflected pressures from the ring at the center, but this is not representative when plate motion occurs since by that time the plate would have moved significantly at the center as will be shown next.

Plate Response

Before considering failure of the plate specimens, it is instructive to describe the typical response of the plates that did not tear to have a good grasp of the events that eventually

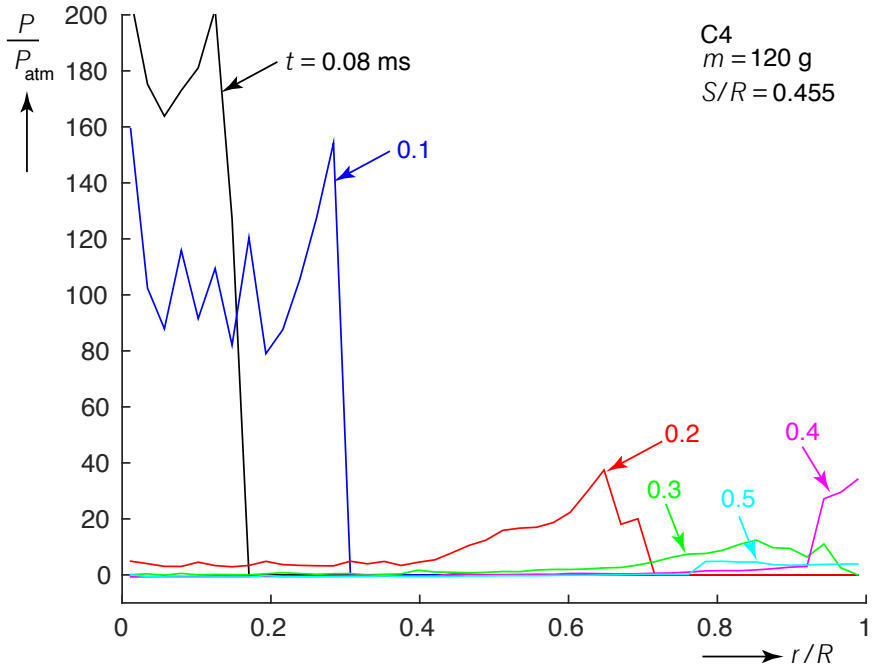

Figure 5. Predicted pressure histories for a C4 charge with mass of 120 g on a plate of radius $R = 22$ in. at a standoff distance $S/R = 0.455$ for the time period $0 \leq t \leq 0.5$ ms.

will lead to failure. To accomplish this objective, the response of a plate with thickness of 0.040 in. ($R/t = 550$) will be described next.

Figure 6(a) shows a series of displacement profiles obtained from one of the tests where the charge mass was 359 g (0.791 lb). Here r is the radial coordinate measured from the center of the plate and w is the out-of-plane displacement. They are both normalized by the radius of the plate R. The profiles were obtained as described in Section 2.2 and are shown to scale in the figure. Displacements for $r/R > 0.9$ are not given because the length of half the subset size was $r/R = 0.08$, which prevents measurements closer to the edge of the plate. The time period considered is $0 < t < 1.25$ ms, where $t = 0$ represents the initiation of the detonation. The time difference between the profiles is $\Delta t = 0.056$ ms. During the time period shown, the deformation of the plate is essentially axisymmetric. Axisymmetry is lost for $t > 1.25$ as will be discussed later. Figure 6 (b) shows the out-of-plane deflection measured at a radial distance $r/R = 0.018$, which is essentially the center of the plate. This displacement is denoted by Δ and is also normalized by R in the figure. Since the slopes of the profiles at the center of the plate are flat, Δ will be referred to as the displacement at the center of the plate.

The response of the plate for $0 < t < 1.25$ ms can be divided into four regimes. In the first, when $0 < t < 0.08$ ms the plate remains stationary while the detonation wave front travels the standoff distance $S/R = 0.455$. At $t \approx 0.08$ ms, the detonation wave reaches the center of the plate thus initiating deflection. During the second regime, approximately $0.08 < t < 0.30$ ms, the out-of-plane plate deflection propagates from the center towards the edge as shown by the four green profiles in Fig. 6(a) and the corresponding green circles in Fig. 6(b). The front where the deflection becomes non-zero is in the vicinity of the position of the pressure front propagating radially on the plate surface as calculated in the CTH analysis presented above.

Once the out-of-plane deflection front reaches the edge of the plate, the interaction with the boundary produces a flexural wave that travels from the edge of the plate towards the center as can be seen in the blue profiles in Fig. 6(a). The amplitude of the wave is boosted by the interaction of the pressure pulse with the clamping ring discussed above. The pressure increase is nearly simultaneous with the initiation of the flexural wave. This third time regime, $0.30 < t < 1.08$ ms is characterized by a significant increase of the plate deflections. The fourth time regime, $1.08 < t < 1.25$ ms is characterized by further travel of the flexural wave towards the center of the plate, but a decrease in deflections at the center of the plate and behind the wave as shown in Figs. 6(a) and (b). Figure 7 shows images taken from the high speed video at $t = 0.47, 0.75, 0.97$ and 1.25 ms. These images correspond to profiles and center displacements noted by the numbers in Figs. 6(a) and (b). The progression of the flexural wave as it travels from the edge towards the center of the plate can be clearly seen. Recall that the detonation pressures are essentially extinguished after 0.5 ms, so the motion of the plate after that time is driven in great part by inertia.

The reduction in out-of-plane deflection behind the flexural wave causes a relatively small reduction in both radial and circumferential strain components. Because the material has yielded, the small reduction in the strain components causes circumferential compressive

loads that lead to wrinkling of the plate as can be seen in the image in Fig. 8(a) taken at $t = 1.5$ ms. This wrinkling destroys the axisymmetry that had characterized the plate deflection. Subsequently, the flexural wave converges at the center of the plate as can be seen in Figs. 7(b) and (c). The arrival of the wave to the vicinity of the center of the plate causes a rapid increase in the deflection at the center as can be seen in Fig. 6(b) that peaks at $t \approx 2.2$ ms. After this time, the deflection of the plate remains essentially static as the plate has reached its final shape. It must be noted, however, that experiments conducted with charges with $m = 120$ g exhibit a complete rebound of the plate deflections such that those plates' final shapes were convex towards the location where the charge had been.

The radial and circumferential strain (ε_{rr}, $\varepsilon_{\theta\theta}$) component profiles that correspond to the displacement profiles shown in Fig. 6(a) are shown in Fig. 9(a) and (b) respectively using the same color scheme. The figures show that at early times, the maxima for both strain components are at the center of the plate. The radial strain then becomes largest at a location just behind the peak of the flexural wave. The circumferential strain component remains largest at the center of the plate for a longer time, but eventually it becomes largest in the neighborhood of the flexural wave. Note that the radial strain component during this time is significantly larger than the circumferential component. The profiles in red correspond to the decrease of out-of-plane displacement behind the wave pointed out in Fig. 6(a). From Figs. 9 (a) and (b), it is significant that while the radial strain for $0.4 \leq r/R \leq 0.7$ is not significantly affected by the reduction in displacement, the circumferential strain decreases about one percent thus causing the wrinkles in Fig. 8(a) to appear. Note that the wrinkles are lined up consistently with the development of a compressive circumferential stress in this region. Figure 10 shows plots of the circumferential vs. radial strain component histories at 10 points along the radius of the specimen. Symbols are shown at time intervals of 0.056 ms. As expected, strain histories near the center ($r/R \leq 0.1$) are nearly proportional and equi-biaxial, with greatest growth at short times. At locations further from the center the strain histories become less proportional. In particular note that the faster strain growth for points located towards the edge of the plate occurs at intermediate times under the influence of the flexural wave traveling inwards from the edge.

To conclude this section, Fig. 11 shows the deflection at the center vs. time for 8 specimens, each subjected to detonation by a different charge, ranging from 120 to 500 g of C4. Larger charges cause faster deflection of the specimens and larger displacement magnitudes. Solid lines represent cases where the plates did not tear, whereas dashed lines represent cases in which, from visual inspection, tearing occurred. Interestingly, while charges of 300 g or larger resulted in permanent deflections consistent with the direction of the blast, specimens subjected to 120 g charges rebounded and finished with deflections pointing towards the location of the charge as shown in the figure. Furthermore, note that the slope of the deflection vs. time plot for the 120 g case becomes steeper in the rebound indicating an increasing rebound velocity followed by a sudden stop shown at the end of the curve. Indeed, in several tests with 120 g charges the plates tore at the center at this time. This failure, however, is beyond the scope of the current investigation. Another important feature of the responses shown is that the times when tearing occurred (indicated by the $\times$) are under one millisecond, close to when the first displacement maximum occurred, but well before the time of

maximum center deflection. Plate failure will be discussed in more detail in the next section.

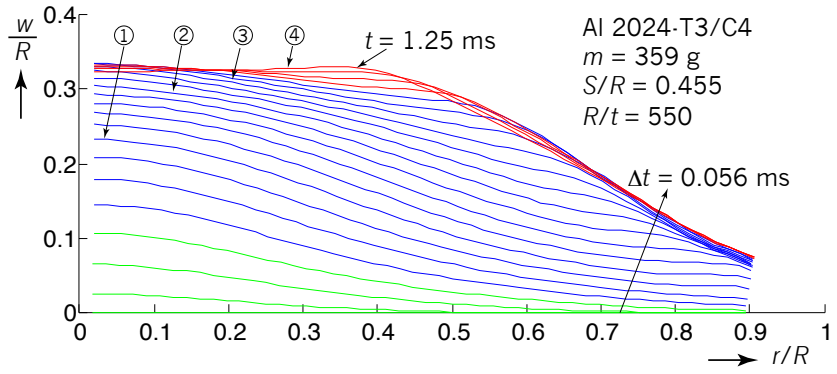

(a)

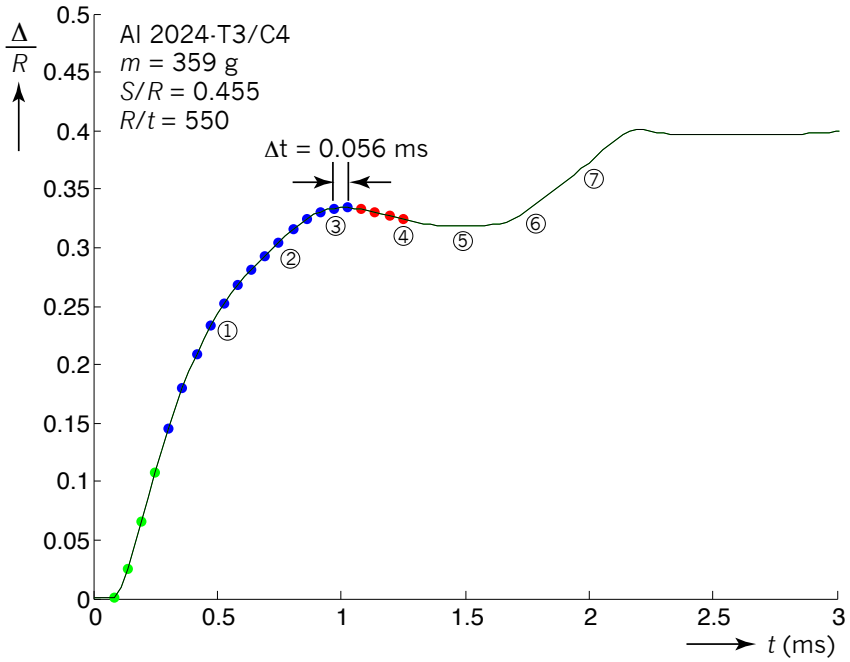

(b)

Figure 6. Plate deflections for a test with $m = 359$ g (0.791 lb) (a) Profiles for the time period $0 < t < 1.25$ ms and (b) center displacement with symbols corresponding to the profiles shown in (a).

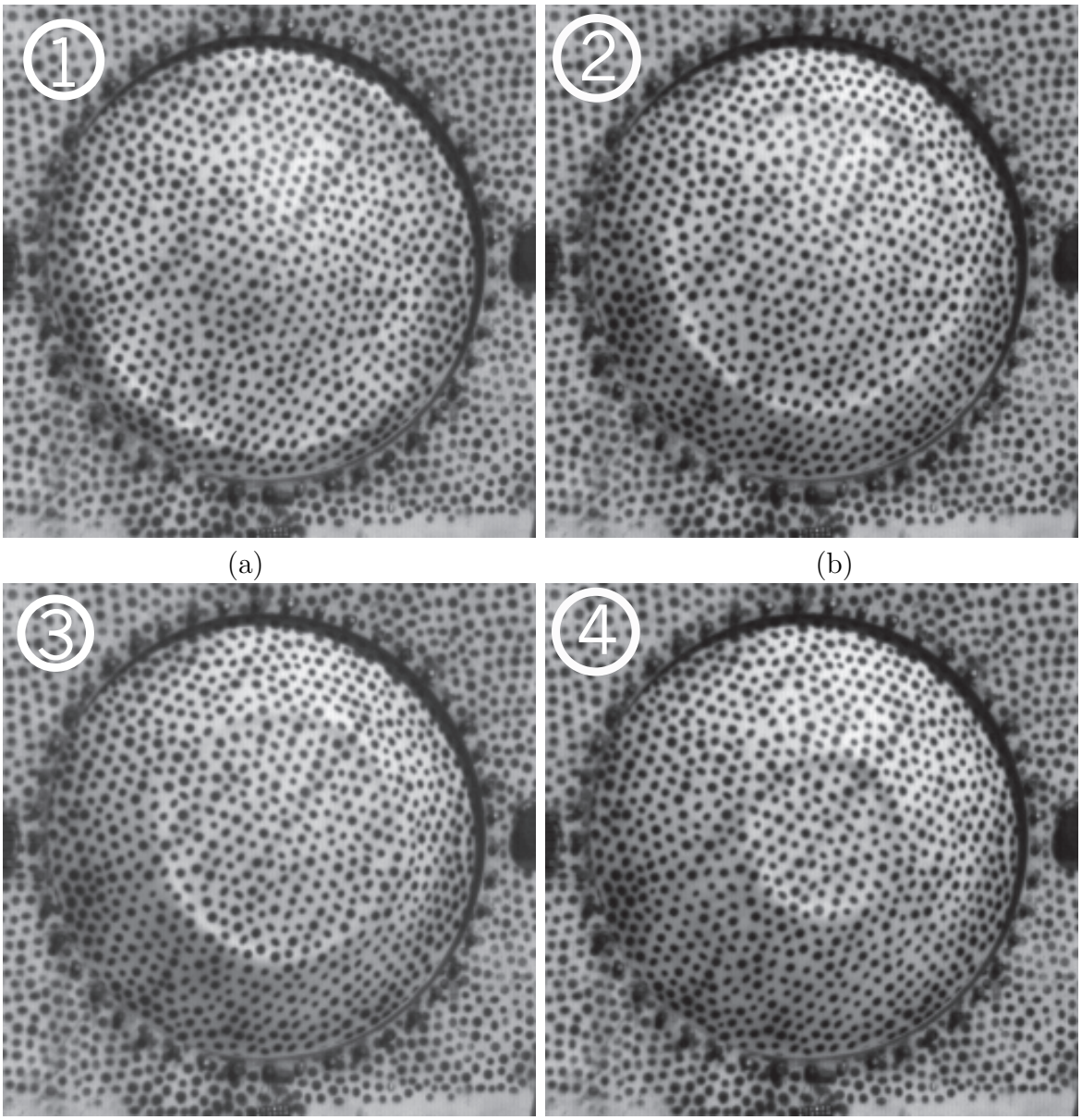

Figure 7. High-speed video images corresponding to the profiles and center deflections numbered in Fig. 6 for $t < 1.25$ ms. (a) 0.47 ms, (b) 0.75 ms, (c) 0.97 ms and (d) 1.25 ms.

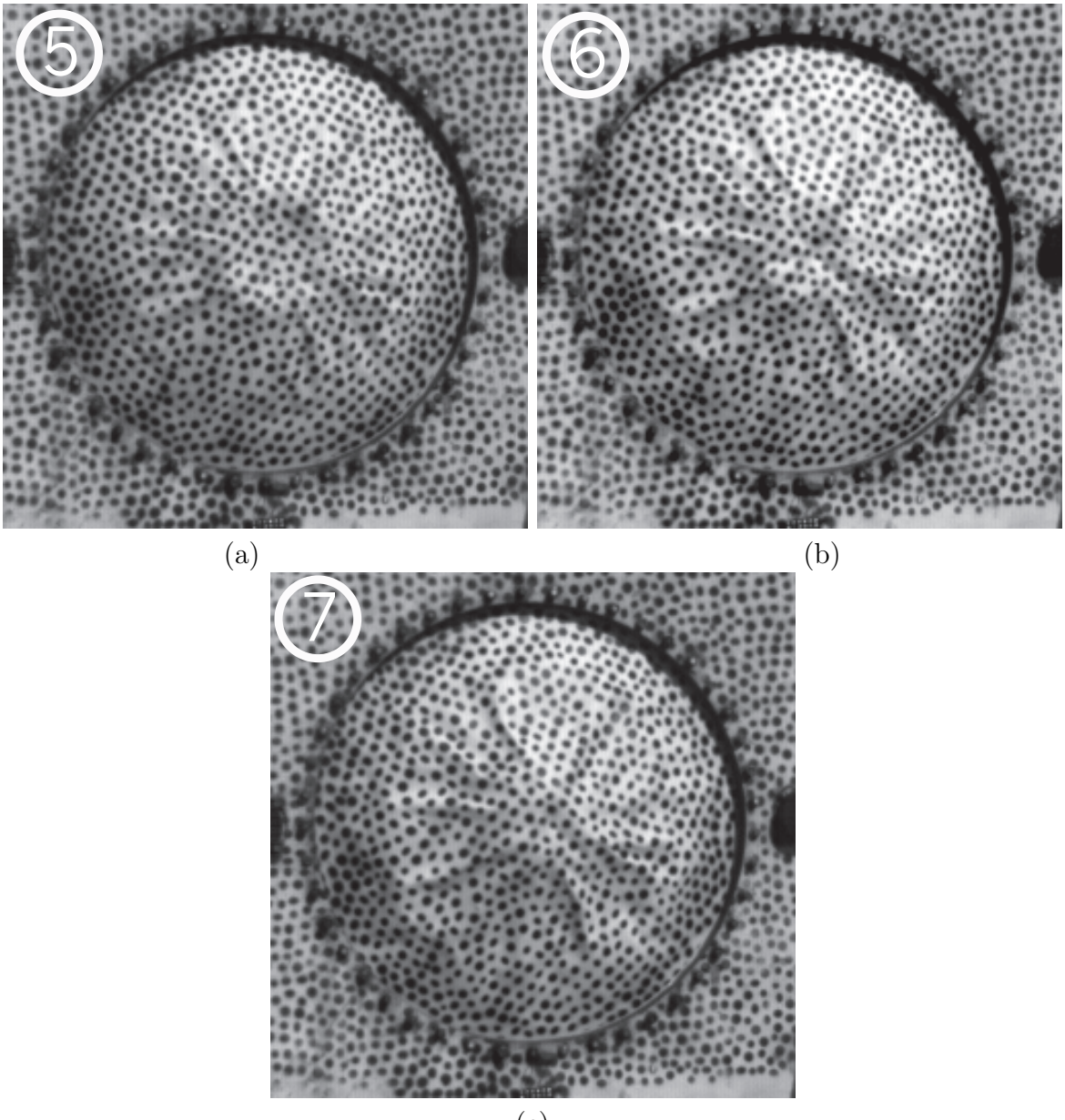

(a) (b)

(c)

Figure 8. High-speed video images showing the shape of the same plate as in Fig. 7 for $t > 1.25$ ms. In particular note the wrinkles that appeared on the plate in this time range. (a) 1.5 ms, (b) 1.75 ms and (c) 2.0 ms

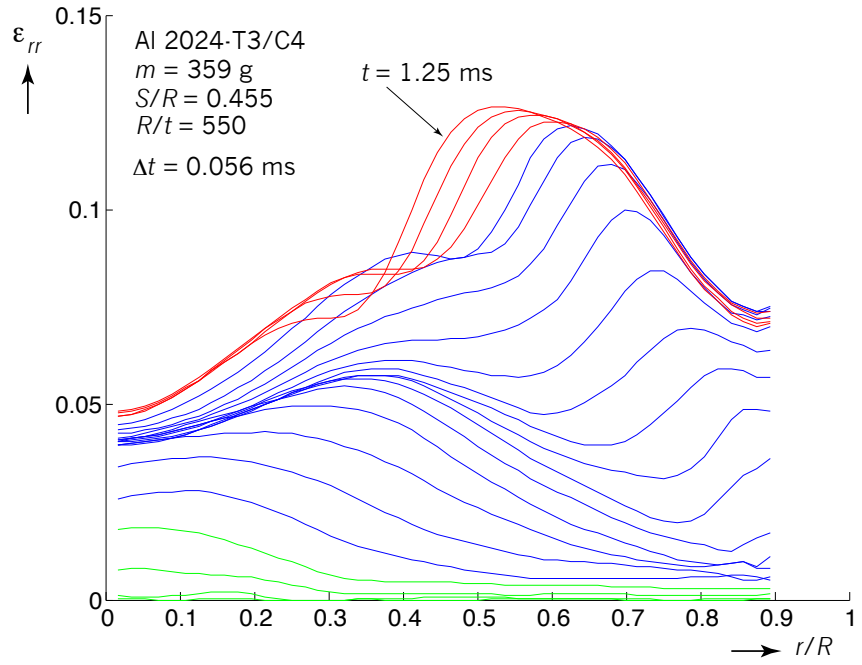

(a)

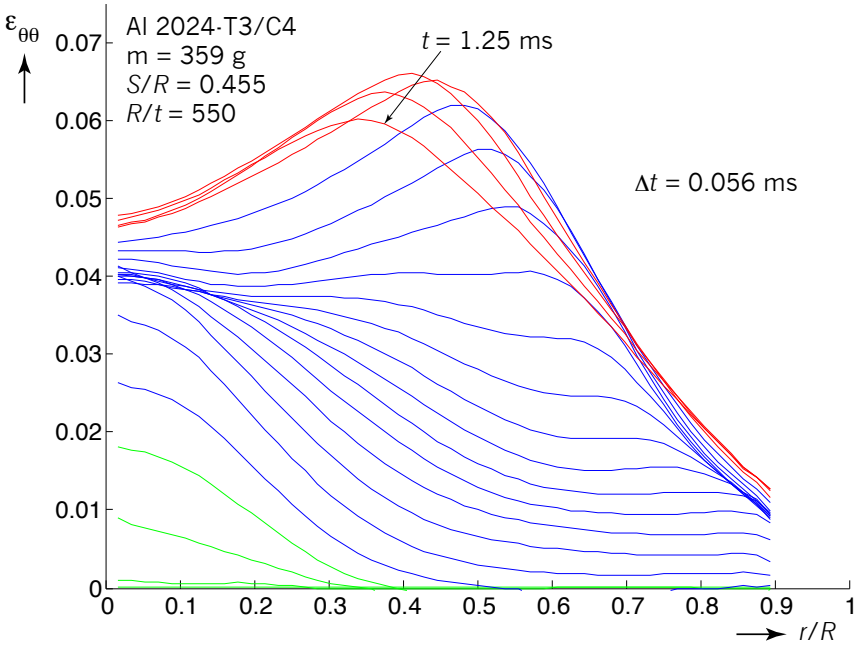

(b)

Figure 9. Plate strain components for a test with $m = 359$ g (0.791 lb) for the time period $0 < t < 1.25$. (a) Radial strain component and (b) circumferential strain component.

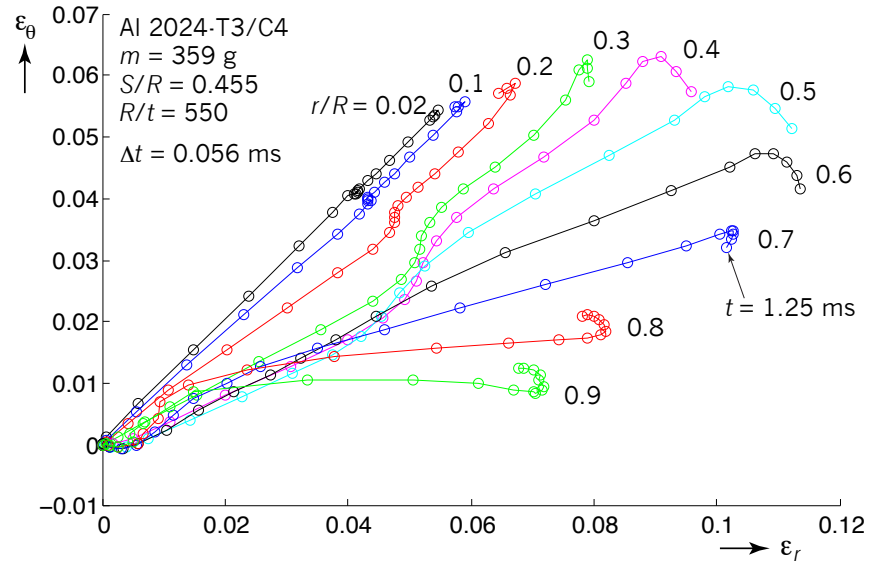

Figure 10. Measured circumferential vs. radial strain histories at 10 points in the plate.

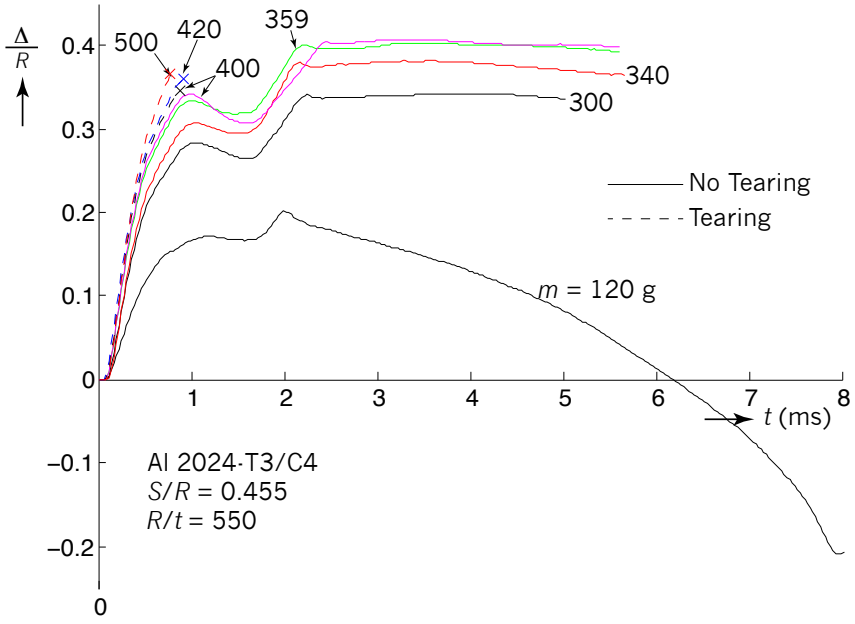

Figure 11. Measured center displacements for all charge masses tested.

Plate Failure

A total of eleven tests were conducted for specimens with thickness of 0.040 in. The order in which the tests were conducted followed an iterative procedure that searched for the minimum explosive mass that caused tearing of the plates. Table 1 lists the tests in order of increasing C4 explosive mass in the first column. The second column lists whether failure occurred or not. If failure occurred, the third column lists the time when failure was detected from observation of the high speed-videos. Finally, the fourth column lists comments relevant to each test. In particular, note the third test with $m = 359$ g and the test with $m = 440$ g (0.969 lb) had unexpected failures. The high-speed video showed that these specimens were hit by fragments, most likely remnants of the detonator, at early times during the tests. Therefore, these results are not valid.

The results listed in Table 1 show that the minimum mass required to tear the plates was in the vicinity of 400 g (0.881 lb). Images showing the incipient failure are shown in Figs. 12(a), 15(a) and 18(a) for tests with $m = 400, 420$ and 500 g (1.10 lb). In all cases, note that the location of first failure was a little behind the flexural wave when it had traversed less than half the radius of the plates. The test with $m = 400$ g simultaneously developed a small crack oriented radially just in front of the wave that is difficult to see in Fig. 12(a). Figures. 12(b), 15(b) and 18(b) correspond to later times and show that the tearing in the plates propagated in a circumferential manner. In the cases with $m = 400$ and 420 g, a flap formed afterwards that eventually tore off the plates whereas in the case with $m = 500$ g the tearing propagated 360° thus detaching a nearly circular disk from the rest of the plate as shown.

Figures 13, 16 and 19 show displacement profiles of the plates up to the time when tearing was detected. The position of the flexural wave when tearing occurred was approximately $r/R = 0.6$ for the 400 and 420 g cases and approximately 0.7 for the 500 g case. Also note that in the latter case tearing occurred earlier, at 0.75 ms. Figures 14, 17 and 20 show the radial and circumferential strain components contours up to the time when tearing occurred. The maximum circumferential strain at failure roughly coincides with the crest (or region of high curvature) of the displacement due to the flexural wave whereas the maximum radial strain, which has much higher magnitude, occurs behind the crest, roughly at the locations where failure is first seen in Figs. 12(a), 15(a) and 18(a). Also, the circumferential orientation of the tearing is consistent with high radial strain. Recall, however, that the strain components were calculated using a virtual gage length of 2.86 in. and the contours were obtained by circumferential averaging. Therefore, the strain contours are approximate, especially with respect to the amplitude and the sharpness of the strain peaks. So while they give reasonable qualitative information regarding the strain distributions, the local strain amplitude in the material in the vicinity of the tears cannot be established from these measurements.

Table 1. Test results for Al 2024-T3 plates with thickness of 0.040 inches ($R/t = 550$).

Mass (g) (lb)	Failure	Time of Failure (ms)	Comments
300 (0.661)	No	-	-
340 (0.749)	No	-	-
340 (0.749)	No	-	-
359 (0.791)	No	-	-
359 (0.791)	No	-	-
359 (0.791)	Yes	0.88	Plate hit by fragments.
400 (0.881)	No	-	-
400 (0.881)	Yes	0.83	Failure started near flexural wave. Propagated 270° and formed a flap.
420 (0.925)	Yes	0.89	Failure started near flexural wave. Propagated 180° and formed a flap. Fig. 15.
440 (0.969)	Yes	0.33	Plate hit by fragments.
500 (1.10)	Yes	0.75	Failure started in vicinity of flexural wave. Propagated 360° and formed a circular disk. Fig. 18.

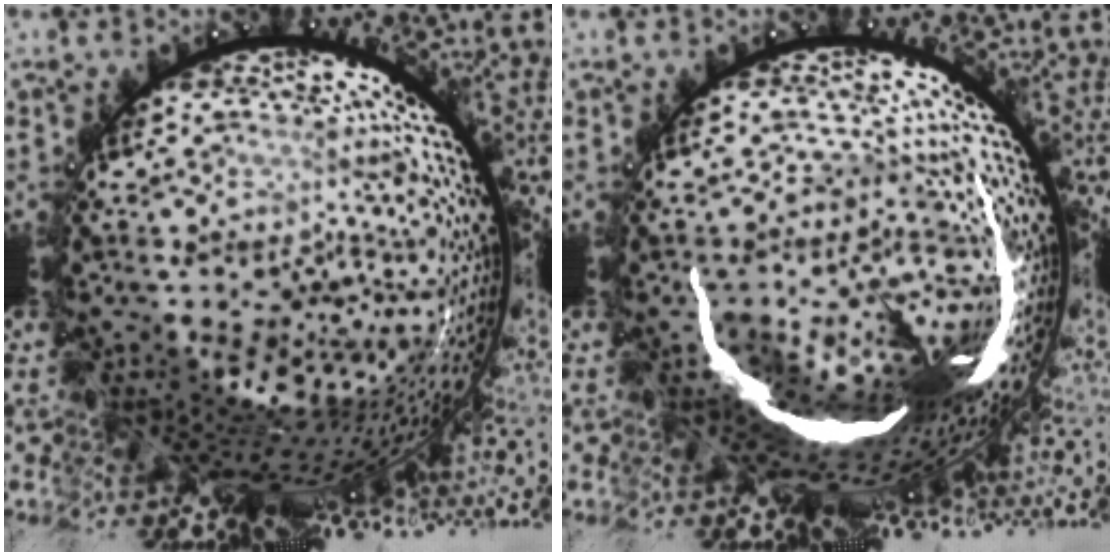

(a) (b)

Figure 12. Plate tearing for $m = 400$ g and $R/t = 550$. (a) Initiation of failure just behind the flexural wave at the 6 and 4 o'clock locations at $t = 0.83$ ms and (b) progression of tearing of the plate at $t = 1.16$ ms.

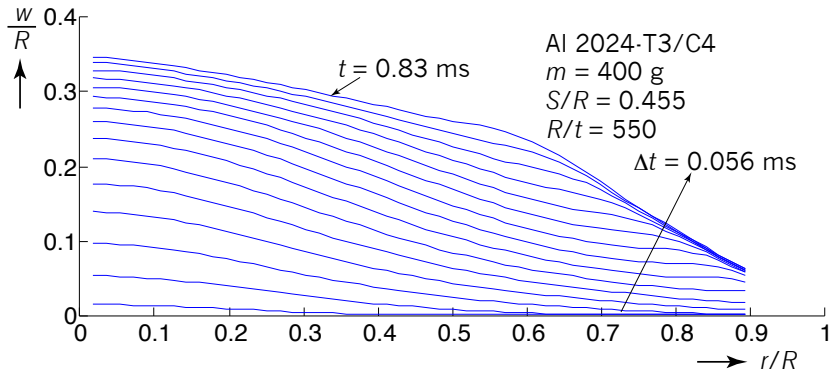

Figure 13. Displacement profiles up to the time of failure for a test with $m = 400$ g.

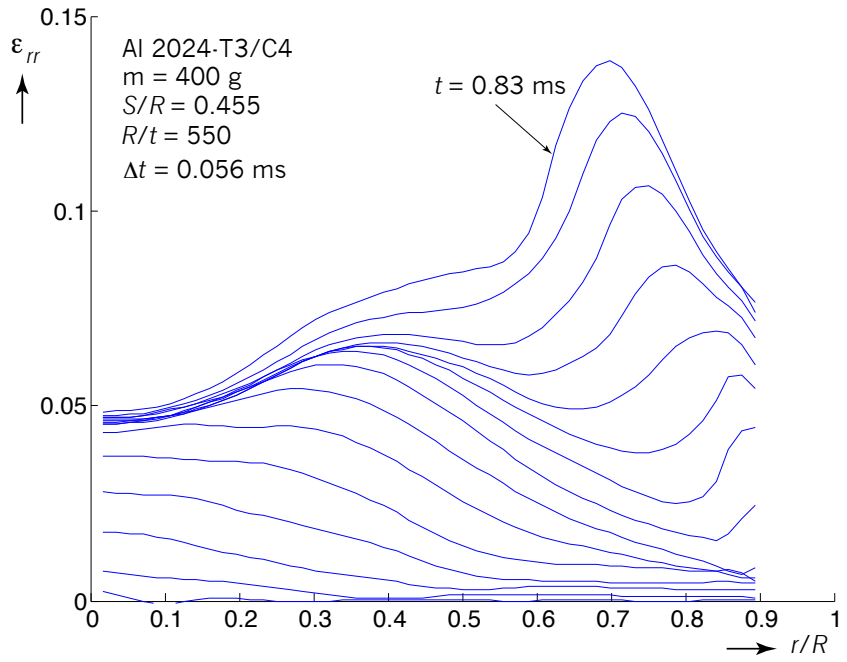

(a)

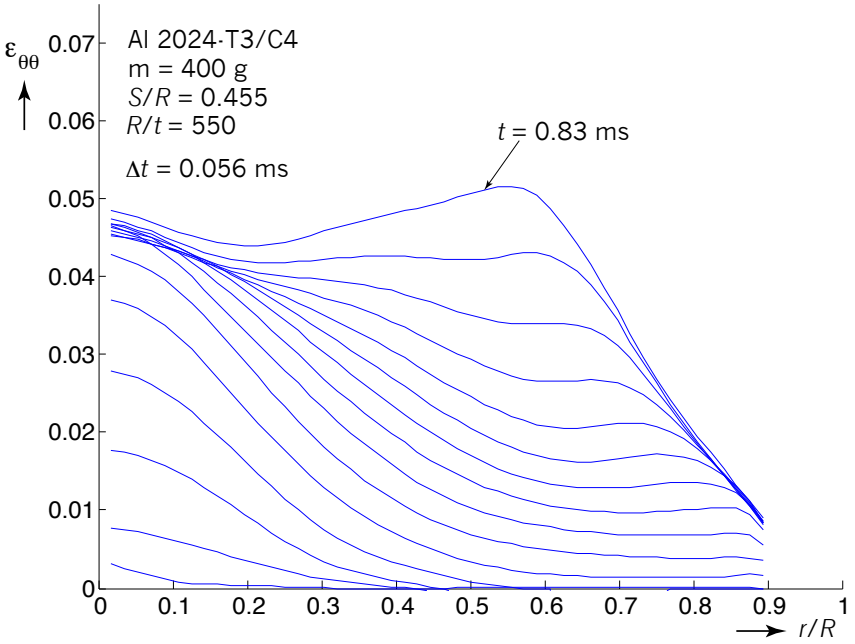

(b)

Figure 14. Strain profiles up to the time of failure for a test with $m = 400$ g. (a) ε_{rr} and (b) $\varepsilon_{\theta\theta}$.

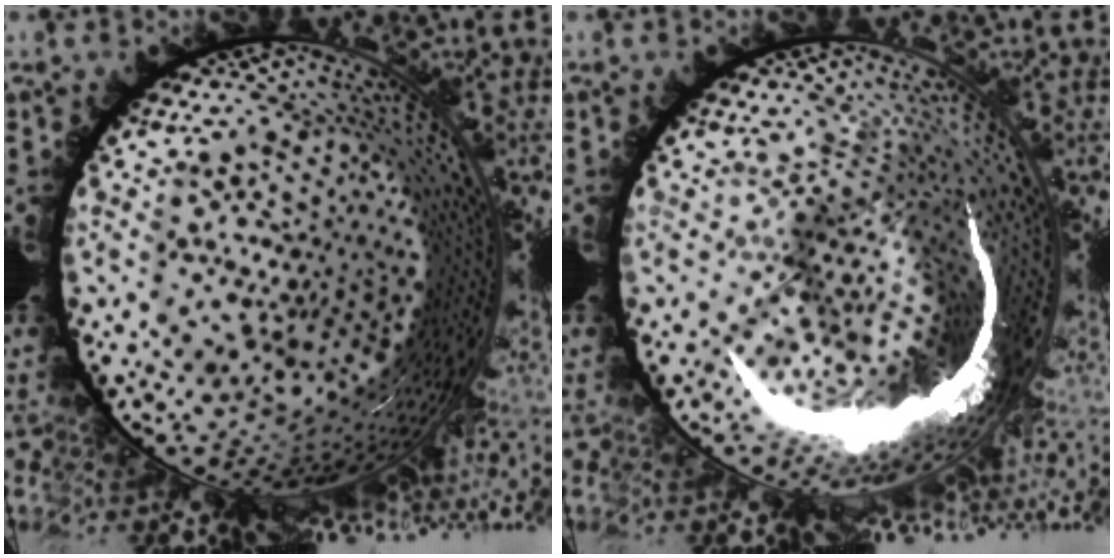

(a) (b)

Figure 15. Plate tearing for $m = 420$ g and $R/t = 550$. (a) Initiation of failure just behind the flexural wave at the 5 o'clock location at $t = 0.89$ ms and (b) progression of tearing of the plate at $t = 1.53$ ms.

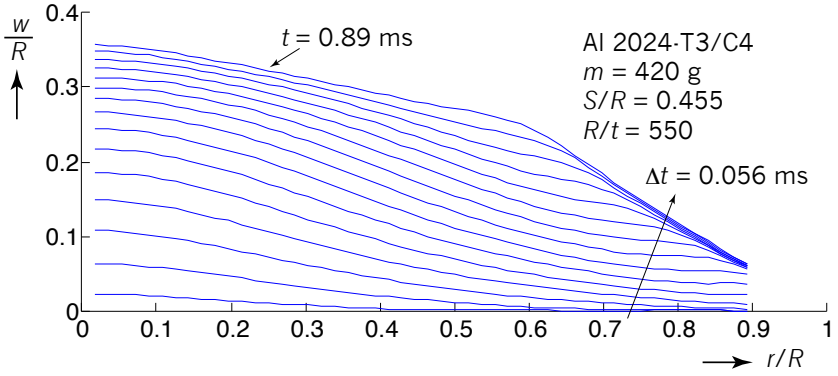

Figure 16. Displacement profiles up to the time of failure for a test with $m = 420$ g.

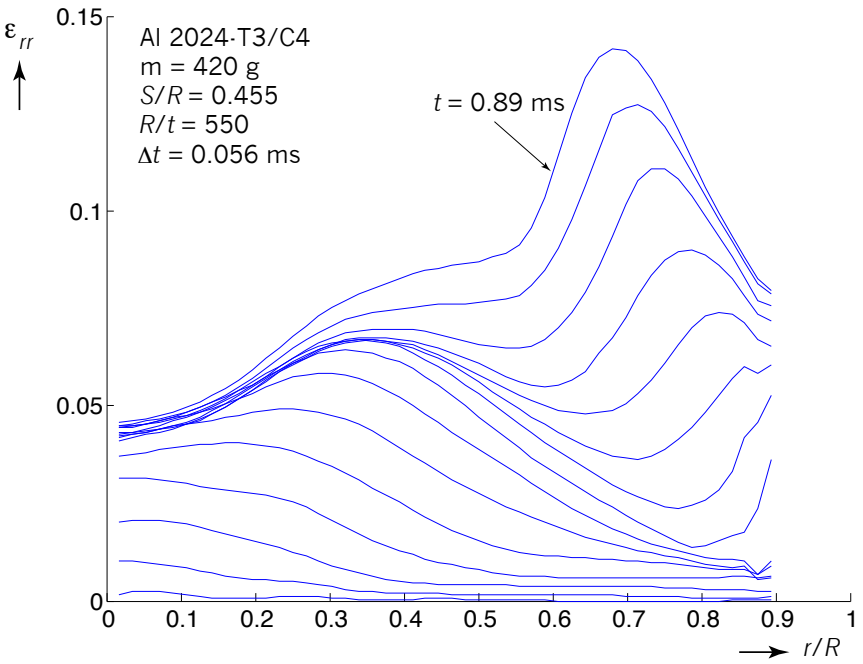

(a)

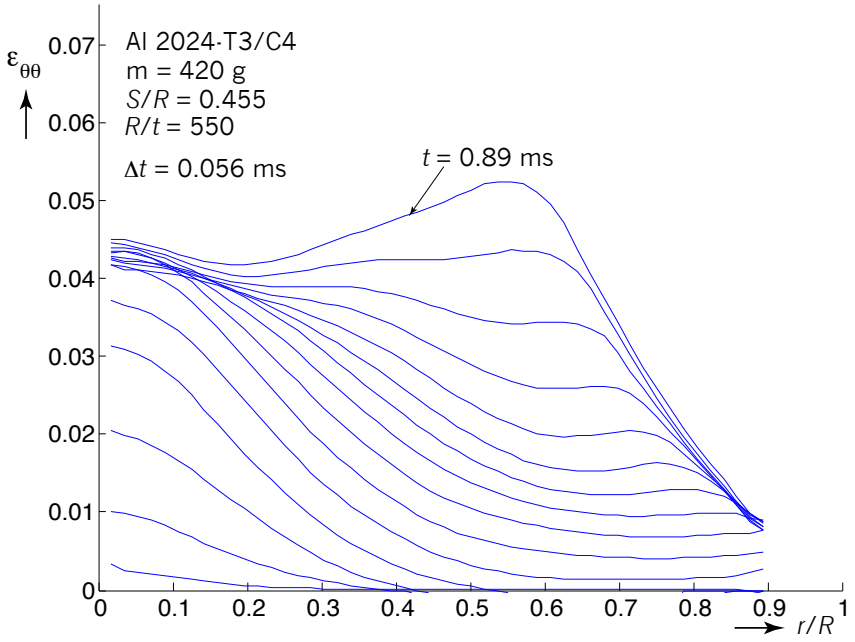

(b)

Figure 17. Strain profiles up to the time of failure for a test with $m = 420$ g. (a) ε_{rr} and (b) $\varepsilon_{\theta\theta}$.

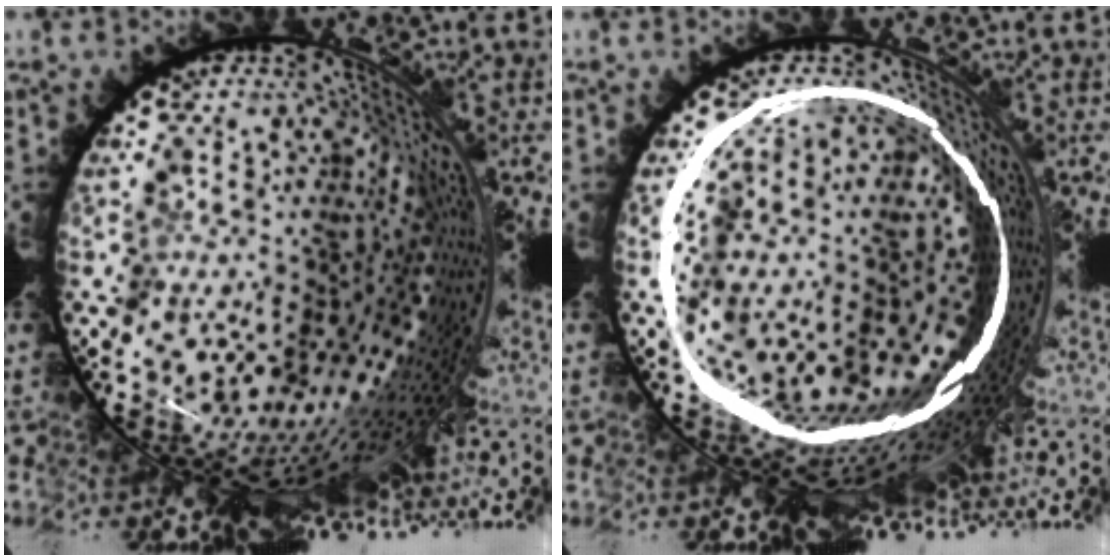

(a) (b)

Figure 18. Plate tearing for $m = 500$ g and $R/t = 550$. (a) Initiation of failure just behind the flexural wave at the 7 o'clock location at $t = 0.75$ ms and (b) progression of tearing of the plate at $t = 0.94$ ms.

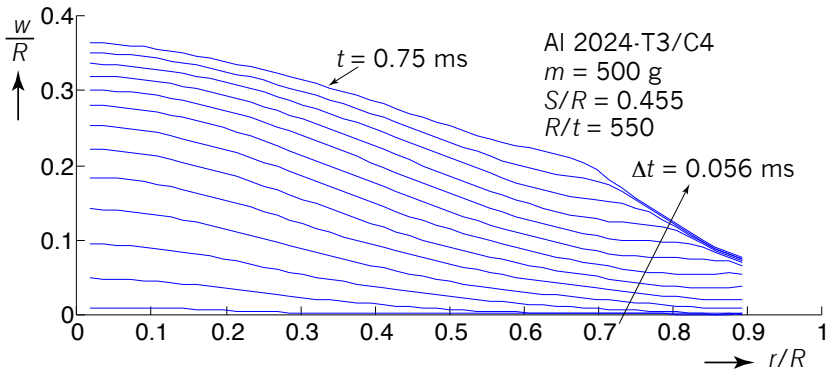

Figure 19. Displacement profiles up to the time of failure for a test with $m = 500$ g.

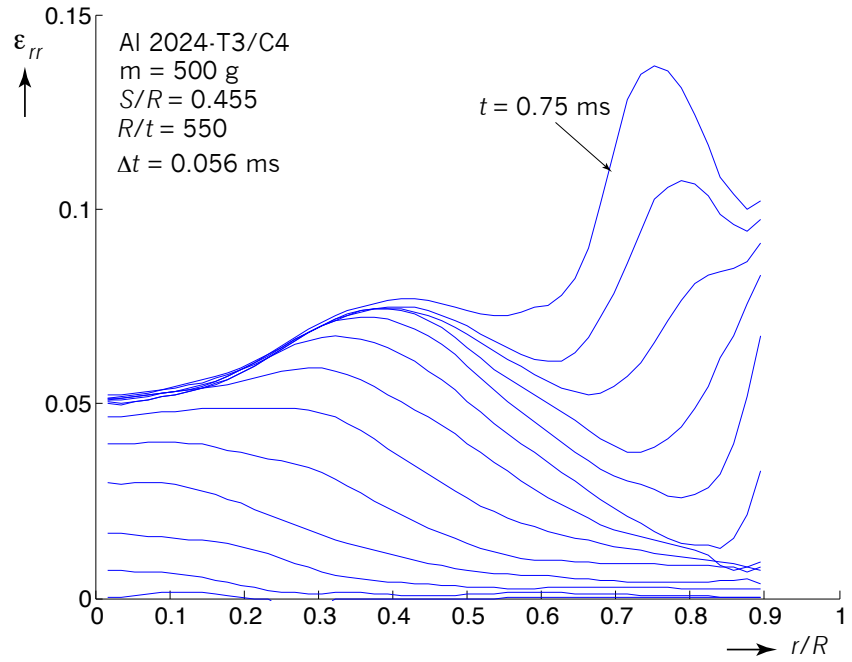

(a)

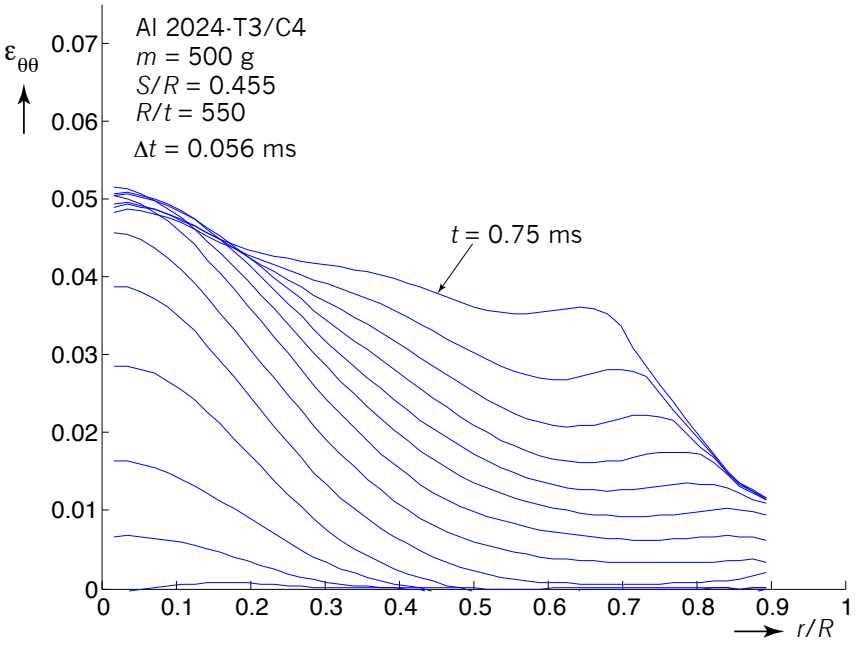

(b)

Figure 20. Strain profiles up to the time of failure for a test with $m = 500$ g. (a) ε_{rr} and (b) $\varepsilon_{\theta\theta}$.

3 Material Characterization for Ductile Failure

Characterization of the mechanical response of the plate material is another aspect of the problem that must be considered carefully. This activity plays an essential role in the present analysis which is to determine the parameters of the material model used. This is of particular importance when attempts are being made to conduct simulations of not only structural response, but of structural failure as well.

The most basic material test that was conducted is the uniaxial tension test. In this test "dog-bone" material coupons were cut from the same sheets used to make the plate specimens that were subjected to blast loading. The coupons were then pulled using properly instrumented uniaxial testing machines in a displacement-controlled manner. In particular, the engineering strain in the specimen was measured using extensometers with a gage length of either one or two inches. Thin sheets, however, develop localized tensile instabilities that result in failure of the specimens at relatively low values of strain as measured by the extensometers used. In other words, the length of the zone in which the deformation localizes is very small compared to the extensometer gage length and therefore the strain measurements are not significantly influenced by the localization.

Higher strain levels can be reached, however, by conducting a "bulge test" on a circular sample of the sheet. In this test the sheet sample was clamped around its circumference and then pressurized as shown in Fig. 21[3]. The diameter of the sheet outside the clamp was 6 in. (15 cm). The pressure was raised by prescribing the volume under the plate using a closed-loop controlled hydraulic system. The deformation of the cusp of the bulge, where the state of stress was equi-biaxial, was tracked using a stereo-DIC system that enabled calculation of the strain components. For more information on the test set-up see the work by Mersch (2013). Using the measured strain components and pressure, it was possible to determine the equivalent true stress-true plastic strain curve of the material (see Appendix B) to strain values of more than twice of what could be determined in uniaxial tension tests (Kyriakides and Mersch, 2013).

Figure 22 compares the equivalent true stress-plastic strain curves obtained from the bulge test to those from uniaxial tension tests. All tests were conducted using sheet from the same aluminum stock with thickness of 0.040 in. used in the current work. In the uniaxial tension curves the axial strain was measured using extensometers with a one-inch gage length. Coupons cut along the rolling direction and perpendicularly to it were tested. Clearly the material showed some degree of yield anisotropy. The end of these curves does not correspond to the failure point. Mersch (2013) indicated that failure occurred at a true plastic strain of approximately 16%, as shown in the figure. The curve extracted from the bulge test data, however, extends to a plastic strain of 28% before tearing of the specimen. The strain measurements were averaged over a region with a diameter in the order of one inch about the center of the specimen (Kyriakides, 2014). The calculations of equivalent stress and strain were based on the von-Mises yield function. Given the anisotropy in the

[3]This experimental set-up was constructed by the Research Center for Mechanics of Solids, Structures and Materials of the University of Texas at Austin with partial support from Sandia National Laboratories.

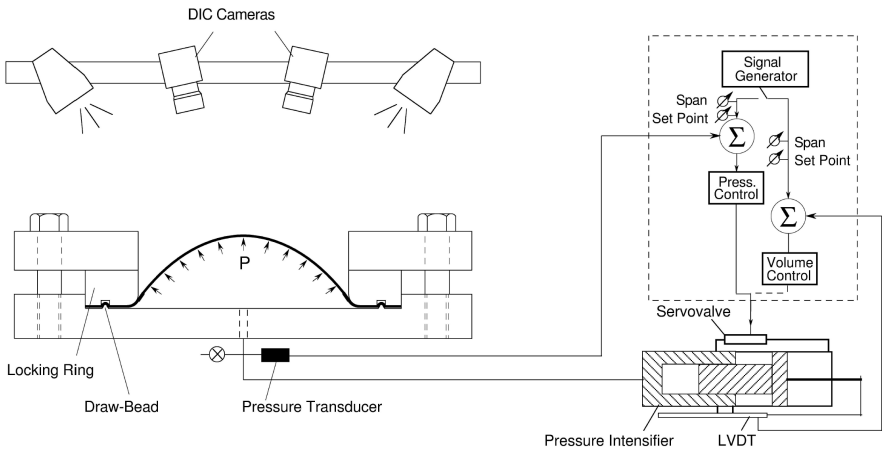

Figure 21. Schematic of the bulge test facility at the University of Texas at Austin. The schematic includes the pressurization system and the DIC cameras. The schematic was extracted from Kyriakides and Mersch (2013).

yield properties and indications in the literature that non-quadratic yield surfaces seem to fit the aluminum alloys better (see, for example, Barlat et al, 2005), this is an approximation. Still, the strain to failure in the bulge test is just under twice that achieved in the uniaxial tension tests. As a final note, failure of the specimen occurred near the clamped region. Experiments conducted after modification of the clamping fixture failed at the cusp of the bulge at equivalent plastic strains in the order of 40%. These tests used specimens of the same alloy and thickness, but from a different lot (Mersch, 2013).

The finite element part of the procedure used to simulate the blast response of the plates modeled the material as an elastic-plastic solid with a von-Mises yield surface that hardens isotropically. The hardening curve of the material must be fitted with a power-hardening law with the form

$$\sigma_e = \sigma_o + A(\varepsilon_e^p)^n$$

in order to be used in the fully-coupled analysis to be presented in Section 5. Here σ_e and ε_e^p are the equivalent true stress and plastic strain and σ_o, A and n are parameters determined during the fitting procedure. Figure 23 shows the fit with $\sigma_o = 45.1$ ksi, $A = 75.6$ ksi and $n = 0.425$ used in the simulations compared to the bulge test data from Fig. 22. The fit does a reasonable job of representing the test results.

Since the response of the plates in the blast tests is dynamic, the dependence of the material behavior at strain rates higher than quasi-static is a concern. The strain rates in the blast tests are in the order of hundreds, excluding any strain localization that may

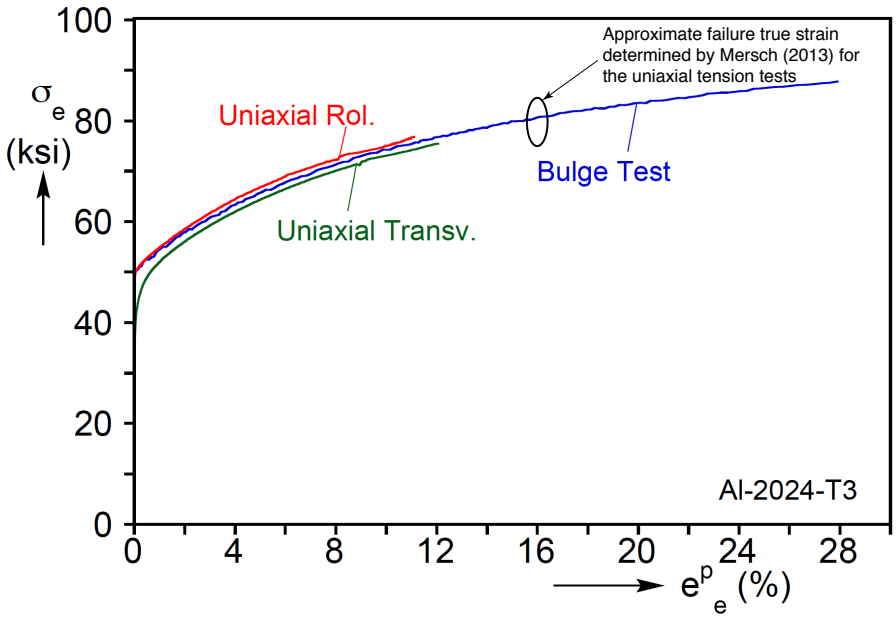

Figure 22. Measured equivalent stress-plastic strain responses of Al 2024-T3 sheet from the bulge test as well as uniaxial tension tests in the rolling and transverse direction. The plot was extracted from Kyriakides and Mersch (2013).

occur for specimens that tore. Data available in the literature point to the conclusion that 2024-T3 aluminum is relatively strain-rate insensitive. Hodowany et al (2000) presented data showing that the flow stress for this alloy varied little between strain rates of 10^{-3} s^{-1} and 3000 s^{-1}. Lesuer (2000) and Kay (2003) presented calibrations of both the strength and failure Johnson-Cook models for this alloy. Their results indicate that changes in the order of 5% for both the flow stress and strain-to-failure can be expected over a three decade change in the strain rate. Strain rate effects were therefore neglected for the rest of the present work.

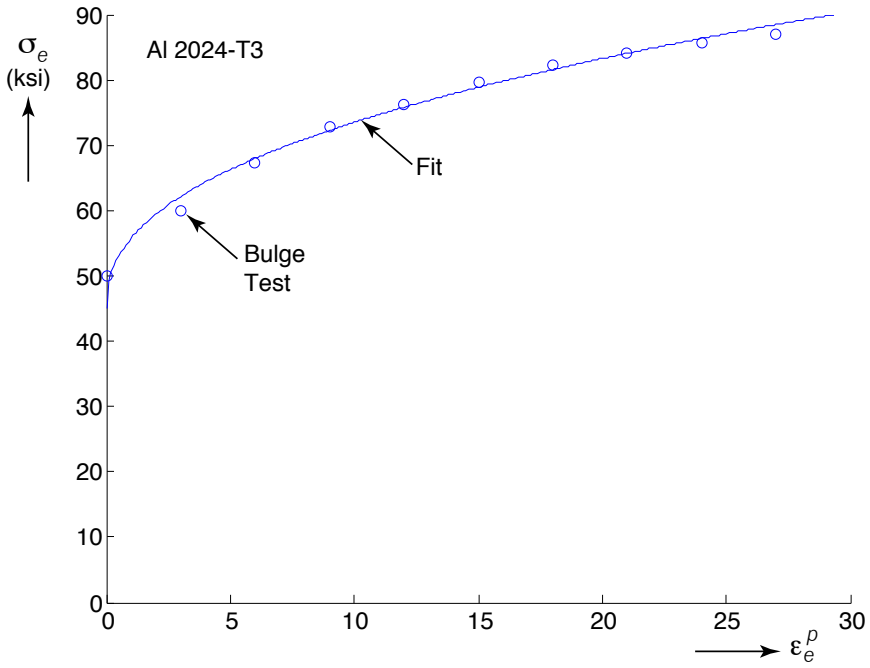

Figure 23. Power law stress-strain fit to the equivalent stress-strain data bulge test data in Fig. 22

4 Computational Blast-Structure Uncoupled Model Results

In Section 1, it was mentioned that an uncoupled blast-structure interaction model was exercised prior to the fully coupled approach used in this work. Plate failure predictions, however, were not correct, even qualitatively. This fact provided the principal motivation to consider fully-coupled approach that will be described in Section 5 with the objective of seeing if the failure predictions can be improved. The uncoupled approach and a sample of the results it produced are the topic of this section.

Figure 24 shows schematics of the previously used uncoupled approach. The blast model is shown schematically in Fig. 24(a). It consists of an Eulerian axisymmetric detonation model implemented in the hydrodynamic code CTH (Crawford et al, 2013). Its objective was to calculate the pressure loading applied to the plate. The model consisted of a domain of dimensions $H \times W$. The domain initially contained air, the spherical explosive charge and the clamping ring of height c. Two of the boundaries of the domain allowed the passage of material using "extrapolated pressure" boundary conditions to prevent reflections. Here, the pressure at the boundary is calculated by extrapolating the pressure from two cells adjacent to the boundary. Symmetry conditions that enforce zero normal velocity at the boundary were prescribed at the two other boundaries. In particular, the part of the lower boundary of length R to the left of the clamping ring represented the plate. A set of tracers was located next to this boundary segment to record the pressure-time histories. A total of 22 evenly spaced tracers was enough to give reasonable simulations. By assuming a plane of symmetry at the location of the plate, the model essentially simulated a blast on a rigid plate. In reality, the plate deflects when subjected to the blast, so one would expect that the pressure at the tracers would be somewhat overestimated. The input to the model included the size of the domain, the mass of the explosive and the parameters associated with the detonation model (programmed burn with a JWL equation of state (Lee et al, 1968) for the detonation products), the size and properties of the clamping ring, the properties of the equations of state for air, and the standoff distance S. Most parameters were fixed for the simulations conducted at $H/W = 2$, $W/R = 1.86$, $S/R = 0.45$ and $c/R = 0.091$, where $R = 22$ in. The length of the sides of the Eulerian cells was uniform at 0.02 in.

Once the pressure-time histories at the tracers had been calculated, they were used to prescribe the load to an explicit dynamics finite element model of the plate with the geometry shown in Fig. 24(b). The model was implemented in Sierra/SM (Sierra Solid Mechanics Team, 2012) using a shell finite element discretization. The model had 22 surfaces in the shape of rings that corresponded to the 22 tracers in the hydrodynamic model. The recorded pressure-time histories calculated at each tracer were uniformly applied to each corresponding ring. The domain in the finite element model had the shape of a square of side $B = 48$ in. All displacement and rotation components in the region outside the circle with 22 in. radius, shown cross-hatched, were constrained. The shell elements used were of the Belytschko-Tsay, four-node type with reduced integration. Five integration points were used through the thickness. Mesh convergence studies showed that elements of size 0.25 in. on their side

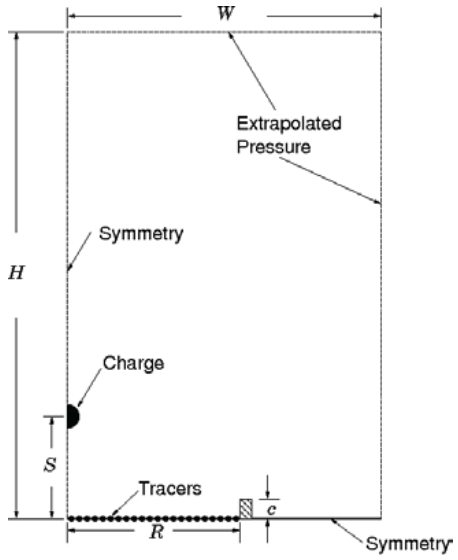

(a)

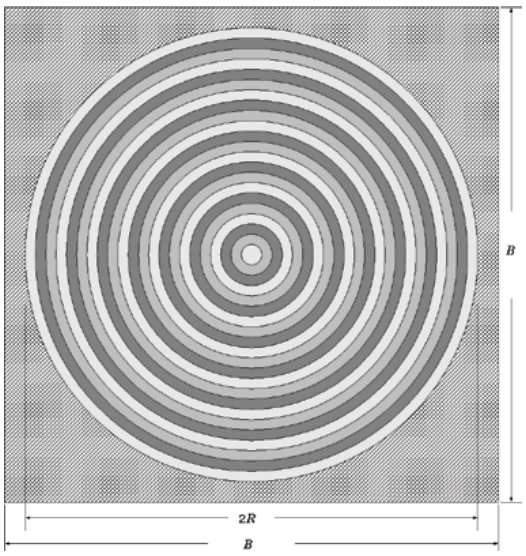

(b)

Figure 24. Schematic of uncoupled models. (a) Blast model in hydrodynamic code CTH and (b) Structural model in the finite element code Sierra/SM.

yielded converged results for the deflection at the center of the plate. All elements had unit aspect ratios. The plate material was modeled as an initially isotropic elastic-plastic solid that hardened isotropically. The stress strain curves of the material used in the experiments was measured through quasi-static uniaxial tension tests and input using a multilinear fit.

Qualitative results of a simulation with charge of $m = 120$ g are shown in Figs. 25(e)-(g) during the forward motion of the plate by direct comparison to the experimental results in Figs. 25(a)-(c). The times of each comparison are given in the caption of the figure. Figs. 25(h) and (d) represent similar configurations during rebound, which occurred at a faster rate in the analysis than in the experiment. Therefore the time in (h) is 2.2 ms less than in (d). The conclusion is that the model simulated the characteristics of the forward motion seen in the experiments very well.

Figure 26 shows a set of calculations of the deflection of the center of plates with thickness of 0.063 in. (1.6 mm, $R/t = 350$) in dashed lines for the mass values indicated. Measurements made in three experiments are shown in solid lines. Although tests were conducted for the two higher charges as well, shattering of the paint on the plates prevented measurements. Lessons learned regarding not letting much time elapse between painting and testing to prevent paint shattering were applied to latter tests. The numerical predictions show excellent quantitative comparison with the experimental measurements during the forward motion of the plate ($t < 2$ ms). The faster predicted rebound is clearly seen for $t > 2$ ms for the lower two charges. The calculated faster rebound is likely a symptom that the pressure differential pushing the plate forward acted for a longer time than predicted by the detonation model. This item will be discussed in more detail in Section 5.

Although the uncoupled model predicted plate deflection very well, its performance in predicting the failure of the plate, even qualitatively, was not satisfactory. The model assumed that failure occurred when a the equivalent plastic strain reached a critical value. One would expect that if the shape and magnitude of the plate deflections were calculated satisfactorily, then the strains would be too, and this was indeed the case, at least qualitatively, for the most part. The calculations, however, consistently predicted an equivalent plastic strain spike at the center of the plate. An example is shown in the plots of equivalent plastic strain vs. radial coordinate shown in Fig. 27. This spike caused first failure to always occur at the center of the plate, something that was not observed in the experiments shown in Section 2.3. This disparity was the main aspect that motivated consideration of the fully coupled approach that will be described in the next section as an attempt to generate plate failure predictions that may be more closely aligned with the experimental results. Another motivation was to determine the effect of the interaction between the pressure pulse and the plate deflection on the calculated deformation of the plates.

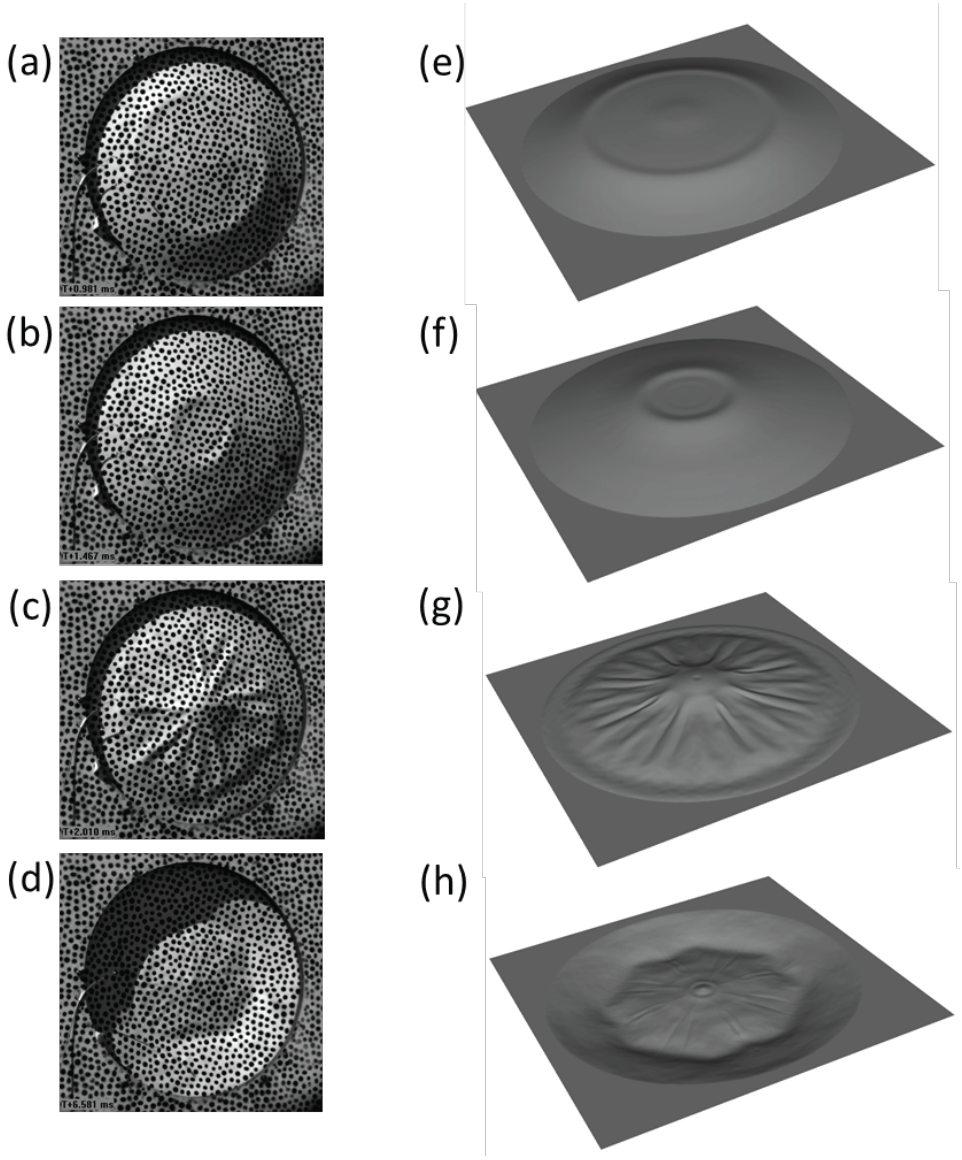

Figure 25. Qualitative comparison between plate shapes recorded in an experiment with a plate with $t = 0.040$ in. subjected to a C4 blast with $m = 120$ g. Experiment shown in (a)-(d) and predictions in (e)-(h). (a) 0.98 ms, (b) 1.47 ms, (c) 2.01 ms, (d) 6.6 ms. The times for (e) through (g) are essentially the same as in (a) through (c). The time for (h) is only 4 ms since the plate rebounds significantly faster in the analysis.

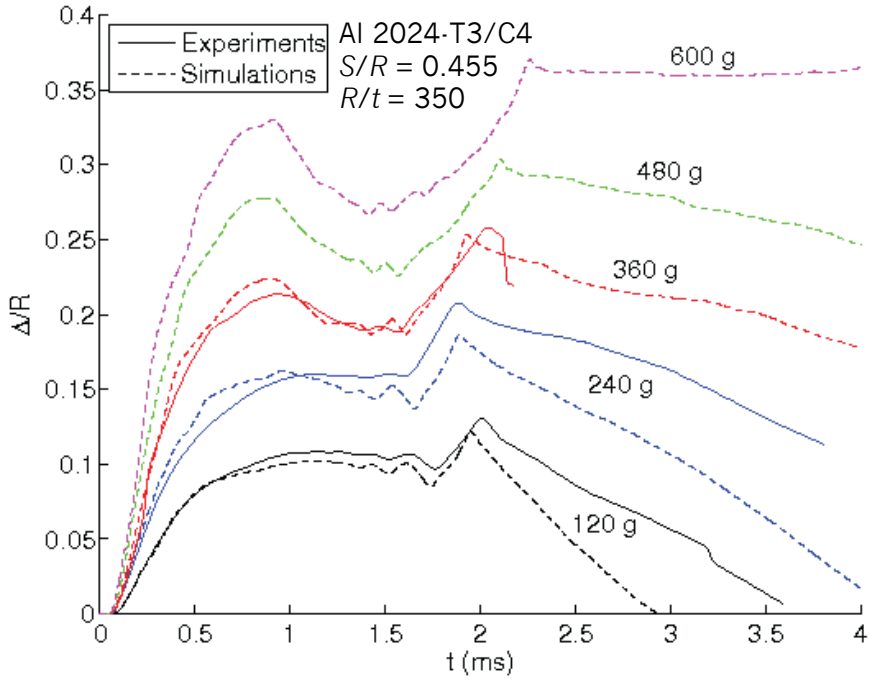

Figure 26. Measured and calculated center plate displacements for a set of 0.063 in. thick plates and various C4 explosive masses.

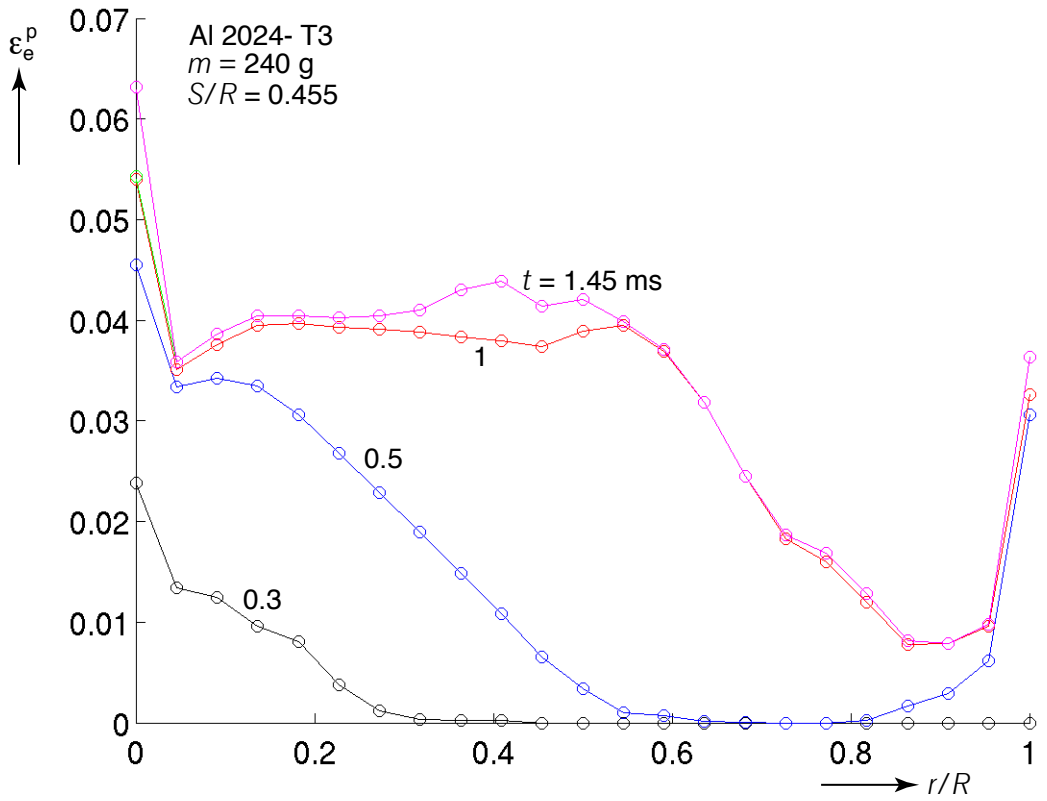

Figure 27. Profiles of equivalent plastic strain typically predicted by the uncoupled approach. Note the spikes at $r/R = 0$.

5 Computational Fully Coupled Blast Structure Interaction

5.1 Zapotec

To explore the plate response further with two-way, or full, coupling, we employed Zapotec (Bessette et al, 2003), a coupled Euler-Lagrange computer code used predominately for defense-related applications. Zapotec directly couples CTH (Crowford et al, 2011), a widely-used Eulerian shock physics code, and a Lagrangian finite element code. Currently, the Lagrangian code used in Zapotec is Pronto3D (Attaway et al, 2000), however the code is currently being updated to use SIERRA/SM explicit also known as Presto (SIERRA Solid Mechanics Team, 2014).

Zapotec employs a unique explicit volume coupling approach that preserves the independence of the separate codes for a set amount of time (typically the size of the CTH time step), and then applies corrections to the simulations to synchronize their solutions before starting a new time step. This synchronization step involves two parts: the insertion of all Lagrangian material into the CTH domain, and the mapping of CTH pressures onto the Lagrangian mesh. In the Lagrangian material mapping step, all previous material corresponding to the last Lagrangian insertion is removed, and the current Lagrangian configuration is re-inserted. Basic information from the Lagrangian solution is mapped into the inserted material, including such quantities as mass and the current stress state. It should be noted that this process resolves any drift in the solution that occurred between the two codes over the time step. To make the Lagrangian side consistent, the CTH stress field from the previous timestep is sampled near the exterior of the inserted material. These sampled stresses are then converted into nodal forces which are applied in the Lagrangian simulation over the timestep. Several different approaches are provided for this sampling to model different interface conditions. In a blast-loaded structure case such as this one, a pressure-only approach is typically used.

Questions regarding the accuracy of the coupling algorithm naturally arise given the explicit nature of the scheme. In a direct sense, the accuracy of the coupling cannot be directly assessed. In other words, no iterations are conducted to ensure that the Eulerian and Lagrangian solutions are within a specific error. With this in mind, a weaker verification of code accuracy is used, comparing the Zapotec solutions to other solutions or test data to see if signifiant errors occur. One such exercise pertinent to the blast-on-plate problem will be demonstrated in Section 5.4.

Zapotec has been used for a wide range of problems both at Sandia and externally. It was originally developed for penetration applications, but has also been used for anti-armor simulations, aircraft impacts, blast loading on buried reinforced concrete structures, structural response to air blast, buried mine blast on structure, space launch failure scenarios, and satellite collisions. More recently, it has been used extensively to model hypervelocity impacts to support lethality assessment for the Missile Defense Agency. Various problems

in these application sets have been compared to experimental data, with reasonable results.

There are a number of code alternatives that also have applicability for the problem set described in this work. At Sandia, the Fortissimo code (SIERRA Solid Mechanics Team, 2013) presents a similar coupling methodology, where the inserted Lagrangian material is treated as a rigid material and where the Lagrangian code is Sierra/SM. Alegra (Carroll et al, 2004) is another Sandia code that provides ALE capabilities for simulating fluid-structure interaction, and the Forte code combines Alegra and Sierra/SM for select environments. Outside of Sandia, Lawrence Livermore Laboratories has developed ALE3D (Nichols, 2011), which has a wide range of ALE-based options. In the commercial code world, Abaqus (Dassault Systemes Simulia, 2014) has developed Abaqus CEL for modeling fluid loading on structures, and codes such as Autodyn (Ansys, 2011) have been developed to simulate blast-and-impact-on-structure problems. Due to limitations in funding and time, only Zapotec will be considered in this work.

5.2 Run Setup

The blast problem was modeled as a quarter-symmetric model to reduce computation time (See Fig. 28). Initial runs modeled the experimental case with $R/t = 550$ and 120 grams of C4, with a 10 in. (25.4 cm) offset from the explosive to the plate.

The test fixture and the plate specimen were modeled in the Lagrangian code (Pronto3D), with shell elements for the specimen and hexahedral elements for the ring and the test fixture, as shown in Fig. 28(a). The specimen was modeled with square elements 0.25 in (6.3 mm) on a side until 4 in. (100 mm) from the center, at which point the elements were graded out to match the coarser fixture mesh. The specimen material was modeled with a rate-independent, isotropic hardening elastic-plastic model that used power law hardening matched to the bulge test data in Fig. 23. The Belytschko-Tsay shell element was used. An elastic model for steel was used for the ring and the test fixture.

The explosive and air were modeled in CTH, with a constant 0.16 in. (4 mm) cell size. The CTH domain is shown in Fig. 28(b) while Fig. 28(c) shows a close-up of the plate region of the mesh so that the Eulerian cell size used can be appreciated. The CTH domain was constructed to be just smaller than the test fixture, with reflective boundaries on the symmetry planes and material outflow boundaries with pressure extrapolation on the other planes. The explosive was modeled with a JWL model to model reacted gases with parameters derived from LLNL (2009), and a programmed-burn model was used to simulate the detonation process. The surrounding air was given a pressure and temperature consistent with the experimental conditions, and was modeled with a sesame equation of state (Hertel and Kerley, 1998). No fracture was permitted nor was a strength model provided for the air or explosive, and no discards were used in the CTH portion of the model.

For the coupling, forces for the Lagrangian mesh were collected using the Zapotec force option 2, which computed forces only from the pressures in the nearest non-mixed cell. The

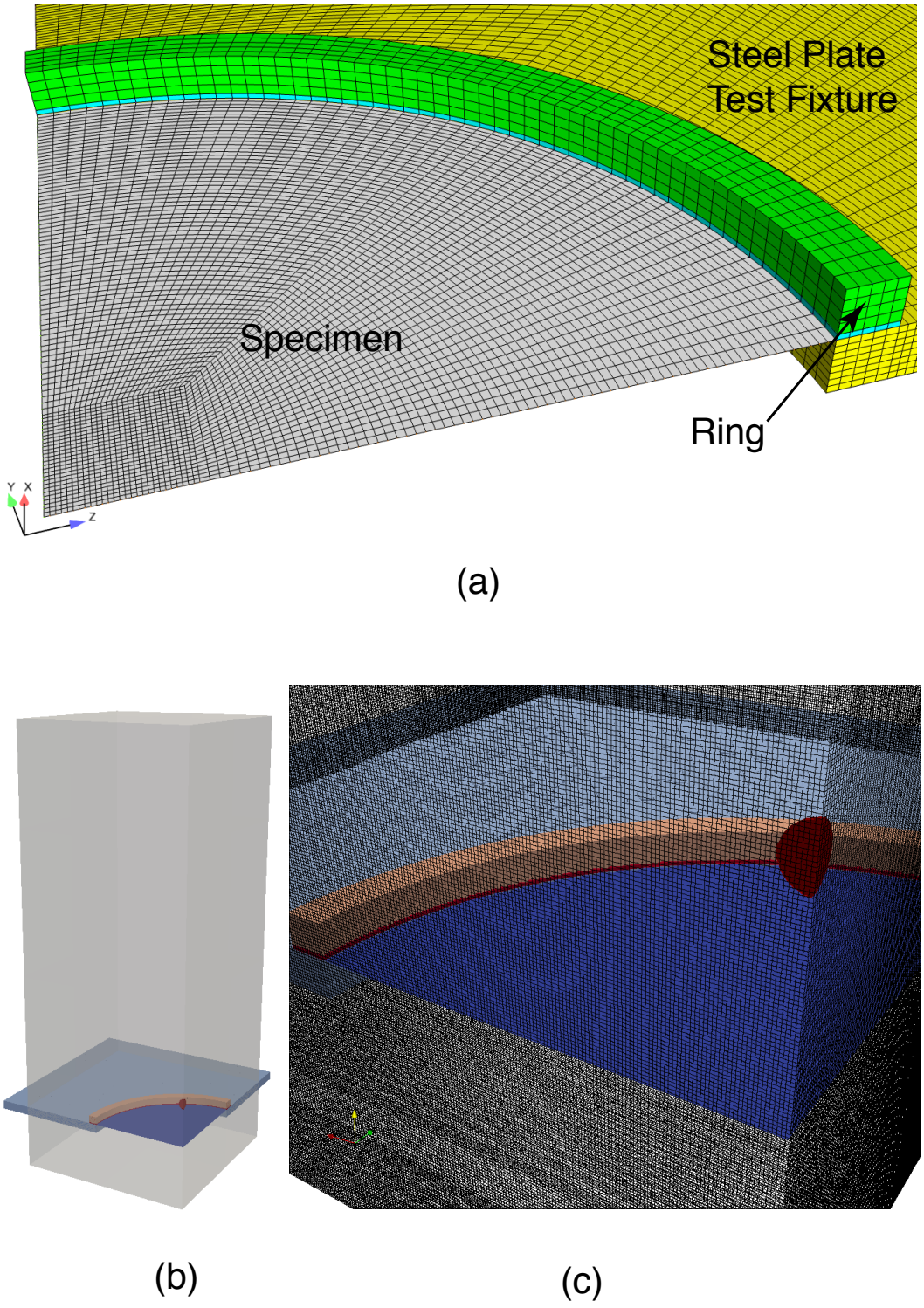

Figure 28. Blast-on-plate problem set-up schematics. (a) Lagrangian Pronto3D domain, (b) Eulerian CTH domain and (c) close-up of of the Eulerian domain showing the cell size.

ambient pressure for the Lagrangian mesh was set the same as the CTH pressure to ensure that the simulation started in equilibrium. These settings, as well as the element size in the Lagrangian mesh and Eulerian cell size had been vetted through other simulations to be best for the structural-blast simulations considered here.

5.3 Initial Results

The results of the baseline run, in terms of the center displacement of the plate as a function of time, are shown in Fig. 29. The plot shows six experimental curves in solid line from six ostensibly identical test setups, along with the results of the baseline run. The tests are split into two series, which differ only by the lot of the sheet used to manufacture the plate specimens. In all cases, the thickness of the plates was 0.040 in. (1.02 mm), giving $R/t = 550$. Of the six experimental curves, three cluster at the top of the experimental range, two lie just below, and a final one lies lower than the rest. Note that the initial slope of the last case is also smaller. This is an indication that the detonation underperformed compared to the others. The simulation results, which assume a C4 density $\rho = 1.56$ g/cc, agree well with the experimental results in the early portion of the curve, specifically it matches their initial slope, but runs just below the lowest experimental result from 0.5 milliseconds on. The simulation results do appear to capture the timing of the secondary bump in the results at 1.8 milliseconds. However, the fact that the results are relatively low bears additional investigation, which is detailed in the next sections.

5.4 Parameter Variation

A collection of computational studies were conducted to explore the sensitivity of the simulation results to input conditions and to identify why the simulation results might be low. The studies explored the sensitivity of the solution to:

- Variation of the JWL parameters used to model the explosive
- Variation of details of the detonation of the explosive (charge size, detonation location)
- Effects of different boundary conditions
- Computational parameters for the code coupling

An additional study considered a much simpler blast problem to explore how effective the coupling algorithm was in capturing similar conditions. Each of these studies is detailed in subsequent subsections.

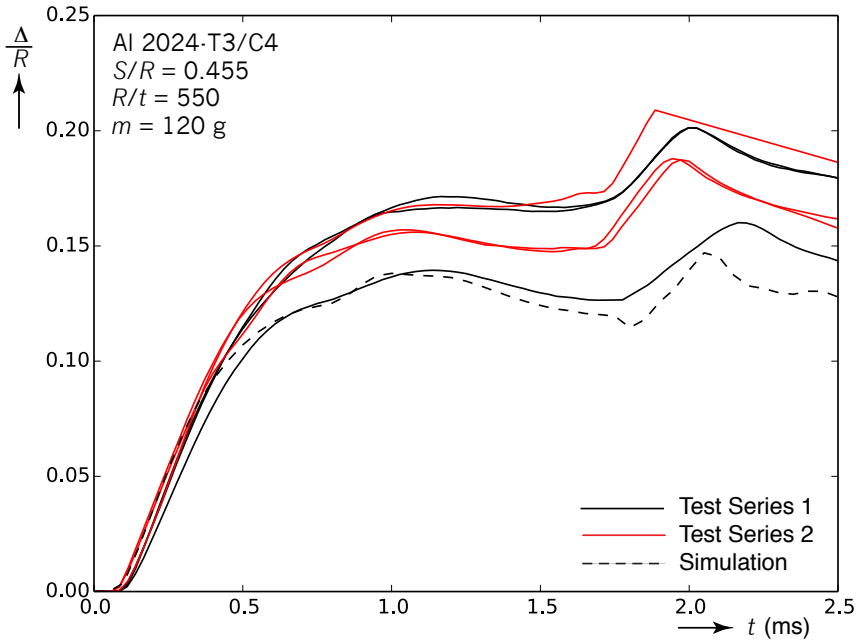

Figure 29. Comparison of 6 measured plate center deflection responses to the initial simulation results. $R/t = 550$, $m = 120$ g.

JWL Parameters

The JWL parameters selected for the initial study came from values selected by a multi-lab team to model this problem. To explore the effect of different fits for this explosive, several additional fits were obtained. Lawrence Livermore National Laboratory maintains an online explosives reference database, in which fits for many common explosives are available (LLNL, 2009). Alternatively, the TIGER code from Sandia National Laboratories can compute JWL parameters from its internal databases (Cowperthwaite and Zwisler, 1973). In both of these cases, simulations were run with all inputs identical to the baseline case except for the JWL parameters. The JWL parameters from the two sources were chosen at several different densities near the density measured of the explosive used for the test; the LLNL fits were chosen at densities of 1.56, 1.58 and 1.60 g/cc, while the TIGER fits were chosen at densities of 1.54, 1.56, and 1.60 g/cc.

Figure 30 shows the center displacement of the plate under blast loading of the baseline case and the five additional JWL fits. The baseline and LLNL cases produced very similar results, while the TIGER fits clustered together slightly below these. However, the variation in center displacement seen from the range of JWL parameters is significantly smaller than the difference from the baseline case to the bulk of the experimental results. This suggests that the specific JWL fit used in the baseline case is not the prime cause of the under-prediction of the simulations.

Variations of Detonation Details

Previous unpublished studies have shown that details in the detonation of explosives can have a strong effect on the impulse delivered to structures. To explore whether the explosive details have a significant effect on the current predictions, several simulations were conducted with variation in detonation location; one simulation initiated the explosive at the point closest to the plate, while the other indicated at the point furthest from the plate. To further explore variations in modeling for the explosive, two more simulations were conducted which detonated in the center but with extra explosive mass – 4 percent (5 grams) and 10 percent (12 grams) larger than the baseline. These variations in mass are clearly beyond the uncertainty in the mass measurements in the experiments.

The plate center displacement for these runs is shown in Fig. 31 along with the experimental data and the baseline calculation. The simulations with the detonation point at the far point of the sphere and the increased explosive masses show only small increases in center displacement. The simulation with detonation nearest the plate shows a marked decrease in center displacement later in time. These results suggest that details in detonation location and in explosive mass have only a minor effect on the plate displacement, and thus are unlikely to be the root cause of the under-prediction of the results.

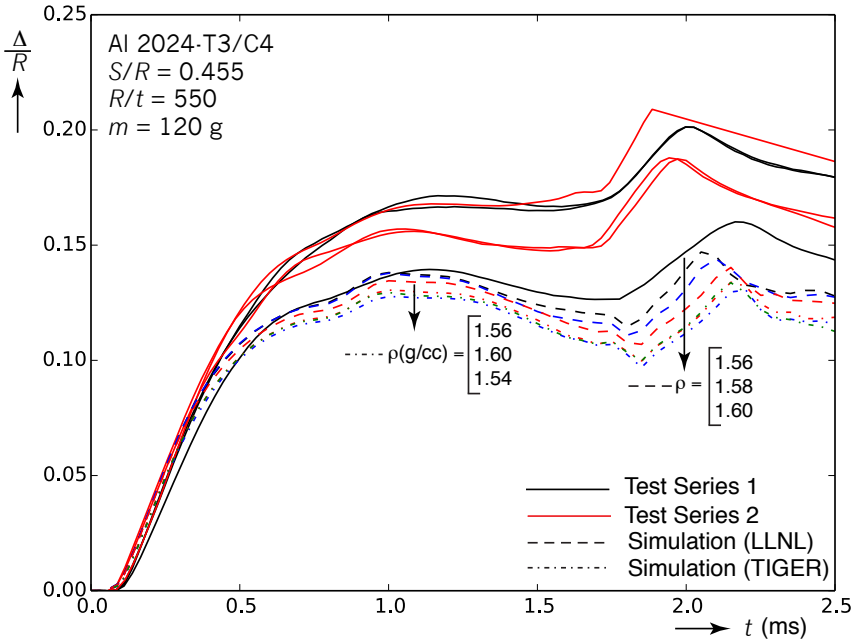

Figure 30. Comparison of 6 measured plate center deflection responses against predictions with various sets of JWL parameters. $R/t = 550$, $m = 120$ g.

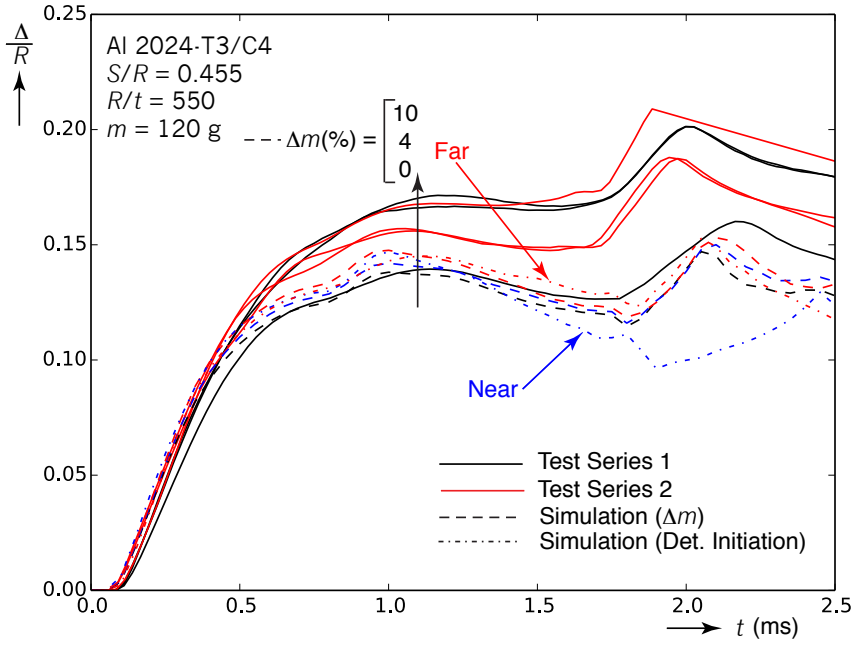

Figure 31. Comparison of 6 measured plate center deflection responses against predictions with increased masses and different detonation locations.

Boundary Condition Variation

The details of how boundary conditions are modeled can have a significant effect on predicted response, thus a series of simulations were conducted with alternative boundary treatments. First, the remote CTH boundaries were altered to be fully reflective. This prevents any material outflow. It should be noted that this approach would lead to inaccurate results after the blast wave reflects off the remote boundary and re-interacts with the plate; however, the boundaries were sufficiently distant that this occurred late in the simulation, after 2 milliseconds. The second simulation kept the original boundary treatment (material outflow with matching boundary pressure), but extended the domain so that the boundaries were 2 times further. A final analysis was conducted with a symmetry plane parallel to the plate through the middle of the explosive. This effectively causes the problem to move from a quarter-symmetric model to an eighth-symmetric model. Note that while this does reduce the domain space of the calculation, cutting the computational cost in half, it does not match the experiment as well. The additional reflective boundary condition eliminates the free expansion of the explosive gasses away from the plate, and can reflect stress waves that can lead to spurious later pressure pulses.

The results from these simulations are illustrated in Fig. 32, which plots the three boundary condition variations along with the baseline case and the experimental data. The first two cases show little to no effect on the displacement of the plate. The use of reflective boundary conditions does show a displacement increase after 2 milliseconds due to wave reflections, but this is outside the main region of interest. The last simulation shows a substantial increase from the other results starting at about 0.9 milliseconds. This jump, however, corresponds to the arrival of a reflection from the added boundary condition. While this result appears to match the experimental data better, it does not represent the free expansion of the experimental conditions, and thus should be discounted. These simulations indicate that the details of the boundary condition models do not strongly affect the results when properly modeling the experimental setup.

Additional Computational Parameters and the Coupling Algorithm

A range of additional studies were conducted to identify whether any other computational details might be the root cause of the under-prediction of the experimental results. These included mesh refinement on both the finite element mesh and the Eulerian grid, which yielded small differences but no substantial increase the predicted displacements. Additionally, Zapotec provides a range of options that control various aspects of the coupling algorithm. Of most importance to this problem are details on how shell elements are inserted into the CTH domain; a multiplier can be applied to increase the effective shell thickness during insertion. In this problem, the true shell thickness is used, but varying the thickness weighting factor so that the insertion occupied up to three CTH cells did not appreciably change the results. Likewise, other coupling algorithm parameters, when set to physically reasonable values, produced little to no change.

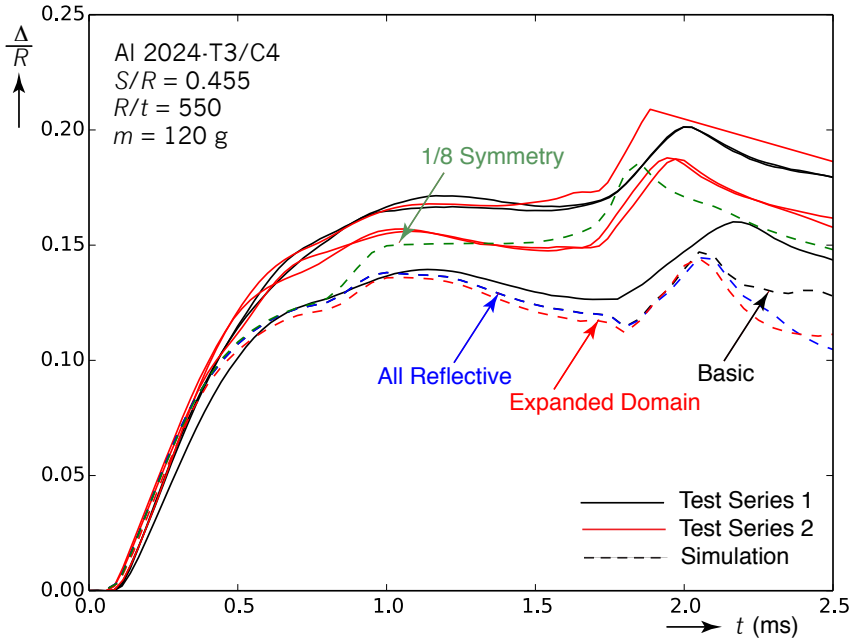

Figure 32. Comparison of 6 measured plate center deflection responses against predictions with different boundary conditions. $R/t = 550$, $m = 120$ g.

Finally, a small separate study was initiated to explore the details of the coupling algorithm. To explore whether the coupling itself provides a pressure that is too low, a simple demonstration problem was created, see Fig. 33. The problem consists of a hexahedral air-filled domain with fully reflective boundaries at standard temperature and pressure, in which a block of solid material is initially at rest. The size of the domain is 10 cm $\times$ 10 cm $\times$ 40 cm, and the size of the block is 10 cm $\times$ 10 cm $\times$ 2 cm. The block has elastic steel properties with density of 7.896 g/cc. At one end of the domain, high pressure air is inserted; this subsequently creates a shock wave that propagates through the domain until it interacts with the block. The wave continues to bounce between the block and the reflective boundary, imparting momentum to the block, which increases its velocity. To test the coupling algorithm, the problem is run in pure CTH, and within Zapotec, where the air domain is kept in CTH and the block is treated in the Lagrangian code. In the Zapotec simulations, the block is modeled with solid elements and with shell elements in separate simulations. To test the effect of different levels of pressure, three versions of the simulations are run at three pressure levels for the high-pressure air: 7, 77, and 770 times greater than standard atmospheric pressure.

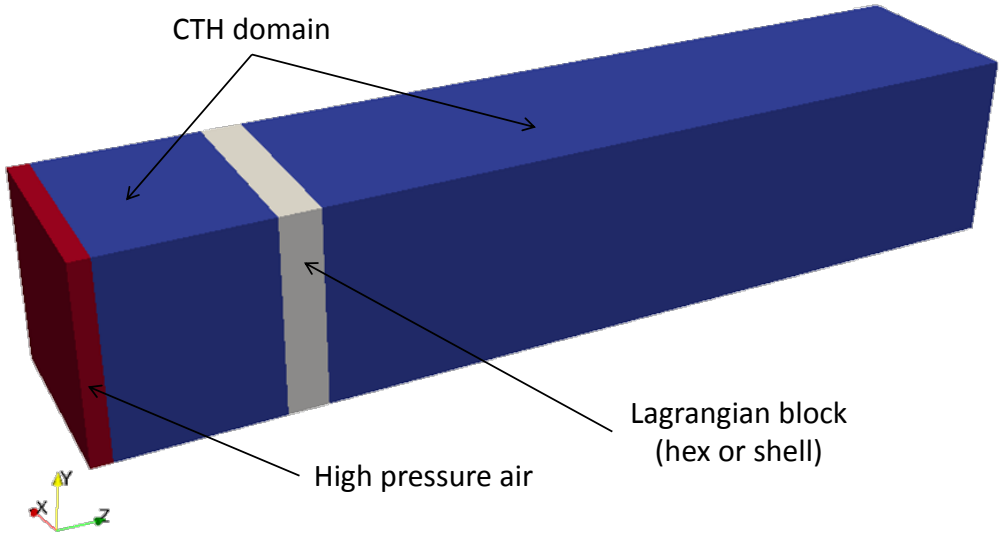

Figure 33. Schematic of simple blast problem used to explore the soundness of the coupling algorithm.

The results of the simulations are shown in Fig. 34. The figure shows the displacement versus time of each of the three cases, with the CTH and Zapotec results plotted on top of each other. In all of the simulations, the difference between the CTH-only solutions and the Zapotec simulations with solid and shell blocks are small. Generally, the Zapotec simulations with solid elements or shell elements are virtually identical, and are within 1% of the CTH solution. Though this is a greatly simplified problem, it suggests that for this application space the coupling algorithm is not losing a significant portion of the loading provided by

the blast wave. This further suggests that errors in the coupling algorithm are not likely to be driving the difference between experimental and simulation results.

Conclusions from Computational Studies

The above computational studies have focused on exploring reasons why the simulation results might under-predict the response seen in the experiments. These studies included changing the parameterization of the JWL explosive model, varying the location of detonation and of the charge mass to explore the effect of initiation effects, boundary condition type and distance, a range of coupling computational parameters, mesh refinement, and finally errors potentially present in the coupling algorithm. In all these studies, the choice of physically reasonable values for these variations produced changes that were well below the difference of the baseline simulation and the experimental results.

Though it is possible that the differences are caused by computational errors that have not been identified, it is also possible that the simulation is missing some physics that is affecting late-time deformation of the plate. In a separate study, Alves et al (2012a) suggested a variation of the JWL model to incorporate afterburn of the explosive, specifically to better simulate this experiment. The revised model postulated that not all of the explosive was consumed during the initial detonation, and that combustion late in time caused a longer-lasting pressure impulse that better modeled the late-time deformation of the plate. Whereas it is inconclusive that this phenomenon is actually occurring in the test, it does suggest that our general approach may be lacking something to properly capture the experiment.

5.5 Addition of Extra Pressure to Better Match the Experiment

To explore how extra pressure missed by our simulation technique would affect our predictions, two additional series of simulations were conducted and tested against experimental results of plates with $t = 0.040$ in. ($R/t = 350$) and $t = 0.063$ in. ($R/t = 550$). In the first series, a constant multiplication factor was applied to the pressure predictions. This is a "knob" that is at times calibrated to improve the agreement of the simulations with test results. In the second series, a constant (over time and space) additional pressure was added to the predicted blast pressure from CTH. This was motivated in part by the possibility that the detonation products reacted with the ambient air producing an additional release of energy over longer times than the duration of the detonation (sometimes called "afterburn"). In both cases, the additional pressures were varied until the simulations provided a reasonable match to the measured center deflection for the 120 gram explosive setup with $R/t = 550$. The calibrated factor or added pressure were then used to predict deformations for experiments with larger amounts of explosive on a different plate thickness, $R/t = 350$. The ability of the modified results to predict the new experimental results provided an indication of what the underlying cause of the differences might be, and also an (albeit entirely heuristic) approach for enabling reasonable predictions of other explosive amounts.

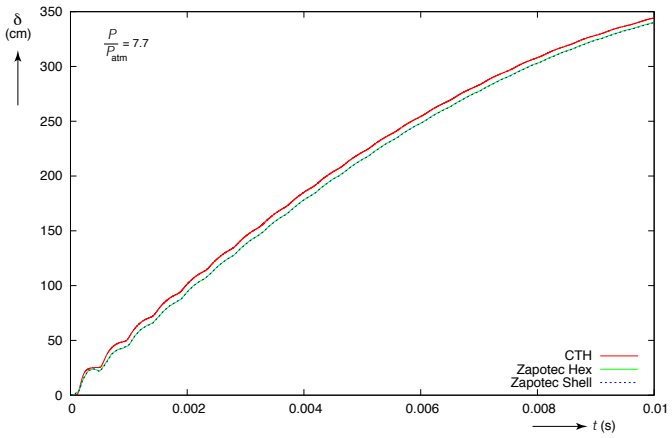

(a)

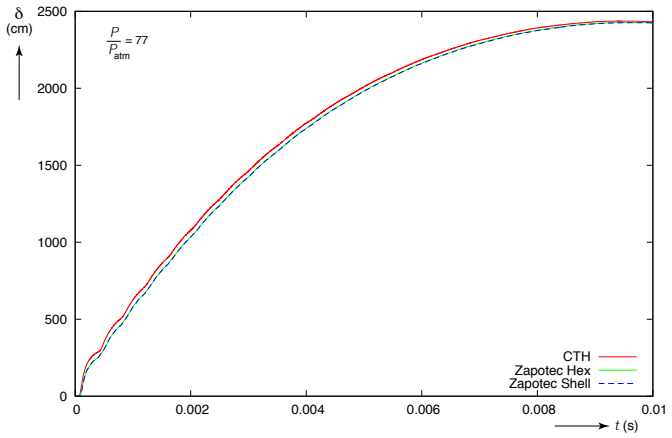

(b)

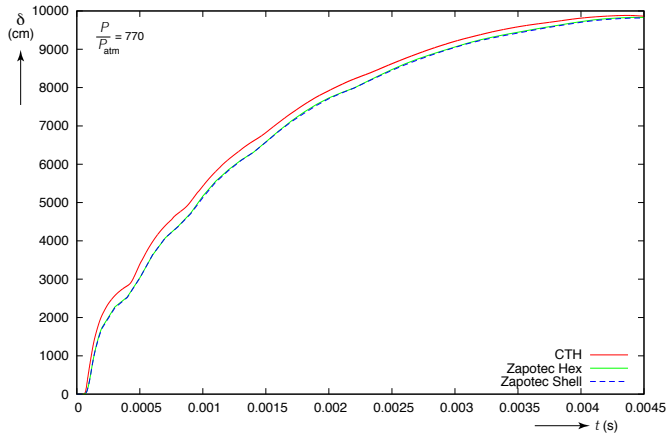

(c)

Figure 34. Comparisons for the motion time history of the solid block in Fig. 33 predicted by CTH, Zapotec with hexahedral elements and Zapotec with shell elements. (a) $P/P_{\text{atm}} = 7.7$, (b) $P/P_{\text{atm}} = 77$ and (c) $P/P_{\text{atm}} = 770$.

Figure 35 shows the results for the first series, where a multiplier is applied to the explosive pressures from CTH. Although none of the multipliers match the curves throughout their length, the value of 1.25 was chosen as a best-fit. Figure 36 shows the use of this multiplier to predict the center deformation of 0.063 in. thick plates subjected to blasts of 120, 240, and 360 grams of explosive. As is clear in the plot, although the new predictions do reasonably well for the 120 g case, they do not match well to the experimental results for higher charges. Generally, the predictions overshoot early-time response (up to 1 ms) and under-predict late-time behavior (1.5 to 2.5 ms). This suggests that a constant scaling is not an appropriate mitigation of the prediction errors.

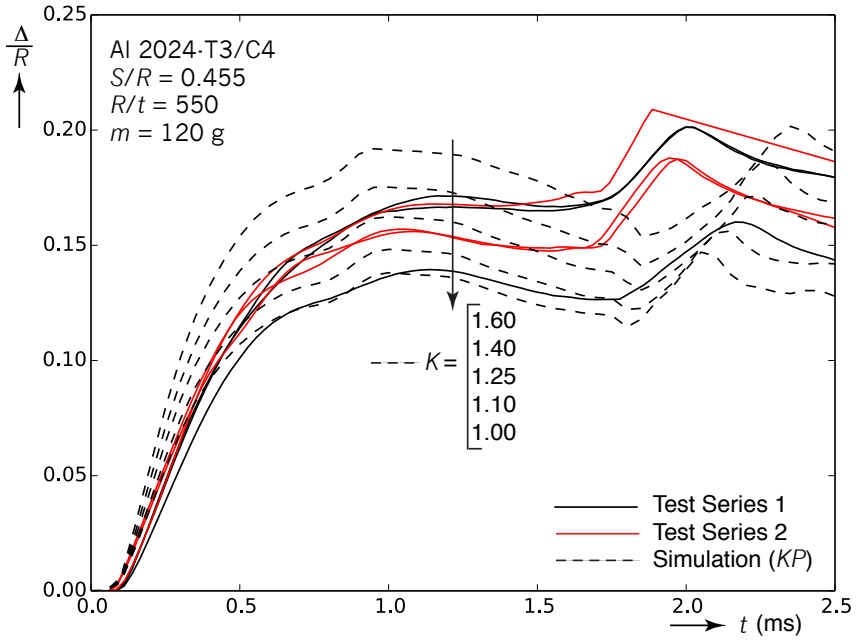

Figure 35. Comparison of 6 measured plate center deflection responses against predictions with varying pressure multiplier values. $R/t = 550$.

Figure 37 shows the results of the second series, where a constant additional pressure was applied to the pressures predicted from Zapotec. In particular, note that the additional pressure was very small compared to the peak pressures predicted by the detonation (see Fig. 5). It does not change the initial slope of the displacement-time response, where the basic detonation model yielded good agreement with experiment. In this case, the addition of a constant 10 psi pressure seems to do a much better job of fitting the experimental results. In Fig. 38, the additional 10 psi is applied to predictions of 0.063 in. thick plates subjected to the blasts of 120, 240, and 360 grams of explosive. In each case, the simulation does a very good job of matching early-time deformation, and a reasonably good job of matching

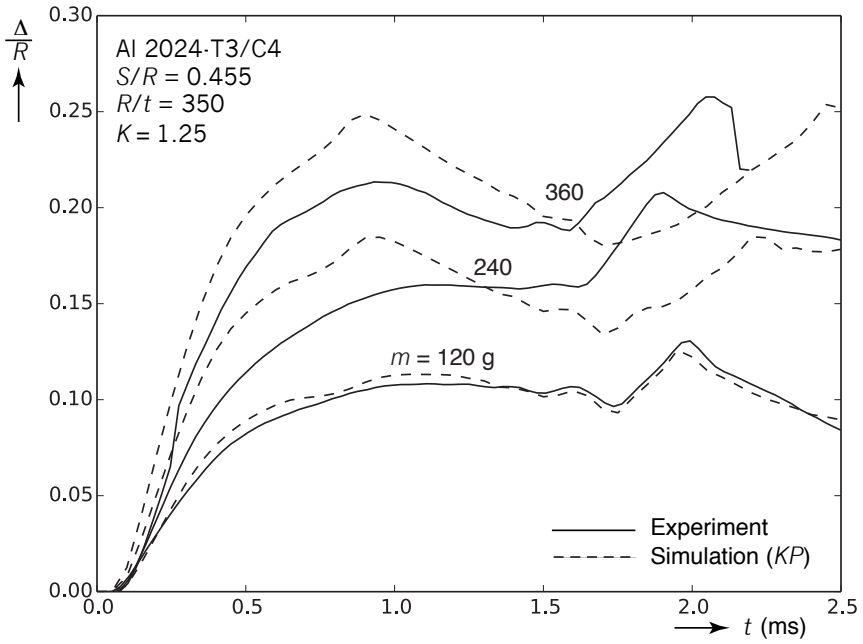

Figure 36. Comparison of the measured center plate deflection for three tests with different explosive masses against predictions obtained with a pressure multiplier value of 1.25. $R/t = 350$.

late-term response as well.

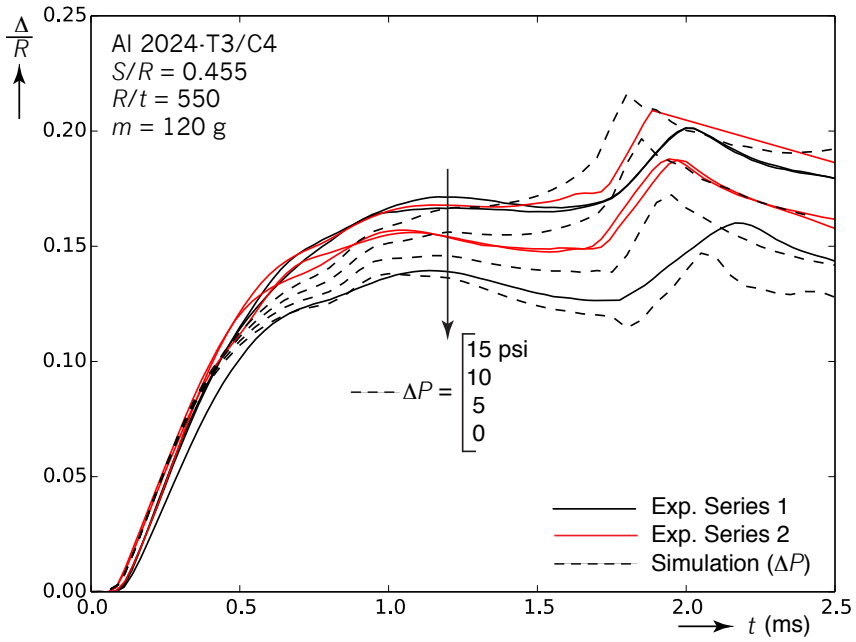

Figure 37. Comparison of 6 measured plate center deflection responses against predictions with various values of additional constant pressure. $R/t = 550$, $m = 120$ g.

Although this study does not prove this, there are reasons to suggest that the modeling approach used in the baseline case could under-predict late-time expansion pressures. One possibility is the afterburn mentioned previously. Another is that the JWL parameters are generally fit from cylinder tests, in which an explosive is surrounded by a metal sleeve and hence the explosive products are constrained to 10-20 times expansion from the original explosive volume. In open air, however, explosive expansion is more in the 100x to 1000x range; hence the JWL fits may not predict large expansion pressures correctly. Further study in better fitting late-time gas expansions holds some promise in enabling better predictions for these plate tests. Further discussion of this point follows in Section 7.

A final series of predictions were performed using the parameters from the baseline run and the extra 10 psi pressure for 40-mil plates subjected to blasts with 300, 340, 359, 400, 420, and 500 grams of explosive. Figure 39 compares these predictions to corresponding experimental data. In nearly all cases, the predictions compare well to the experimental results. These results are used in the remainder of this report.

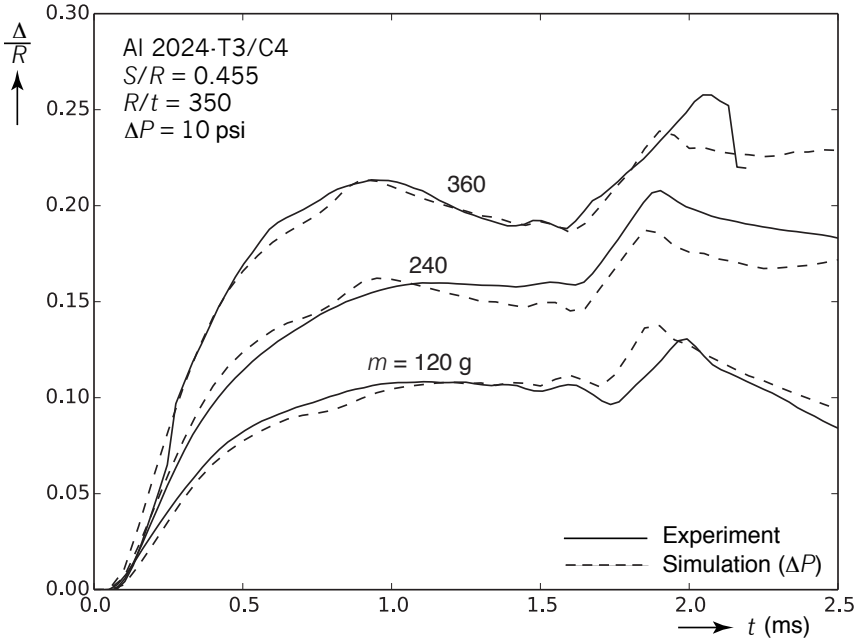

Figure 38. Comparison of the measured center plate deflection for three tests with different explosive masses against predictions obtained with an additional constant pressure of 10 psi. $R/t = 350$.

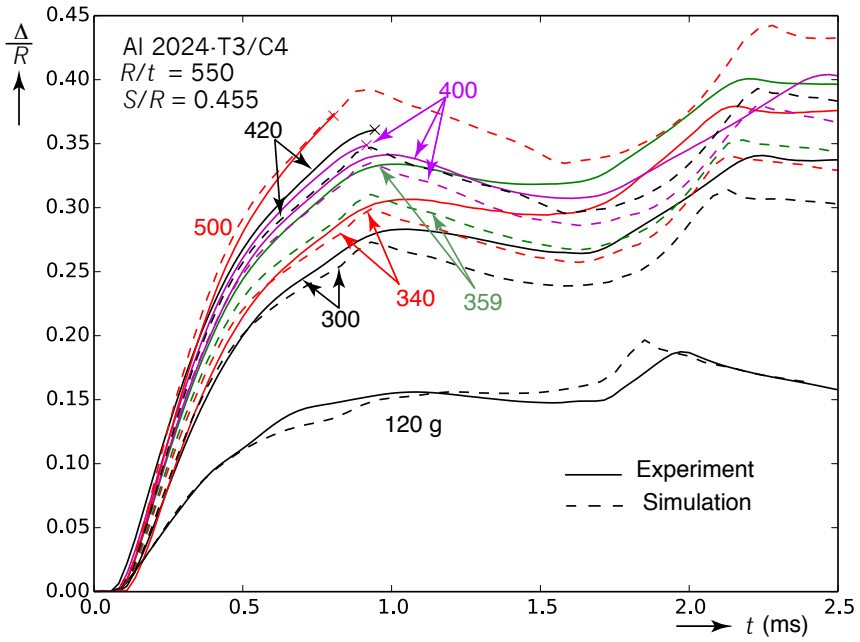

Figure 39. Comparison of the measured center plate deflection for 8 tests with different explosive masses against predictions obtained with an additional constant pressure of 10 psi. $R/t = 550$.

6 Structural Predictions with Current Approach

This section concerns results that look more in detail at the predicted response of the plates using the coupled approach. In particular, Figs. 40 through 43 show plots of four quantities: the plate profiles (a), equivalent plastic strain (b), radial strain (c), and circumferential strain (d) for charges of 359, 400, 420 and 500 g. The profiles in Figs. 40 through 43 (a) can be compared to the measurements in Figs. 6(a), 13, 16 and 19 with corresponding charges.

In comparing experimental to numerical results, note that displacement measurements in the experiments are reasonably accurate, but that strain measurements in regions with high strain gradients are affected by the technique and the size of the strain gage used, as explained in Section 2.2. In the analysis, the profiles are obtained from the nodal displacements, but the strains are calculated from the gradients of the element shape functions and are therefore dependent on the element size. Therefore, the strain plots can not be numerically compared. The trend of the strain distributions in Figs. 40 through 43 (c) and (d), however, can be compared to Figs. 9, 14, 17 and 20(a) and (b) to assess the performance of the model at least in a qualitative manner. Note that while the time increment between profiles is 0.056 ms in the experiments, it is 0.1 ms in the analysis plots. In both cases, however, profiles are shown up until approximately the same time, which was the time just prior to the loss of axisymmetry for the 359 g case and the time of failure for the cases with higher charge mass.

The plate profiles generated in the simulation show reasonable resemblance to the measured ones both in shape and magnitude, thus indicating that the plate deflection calculations have reasonable fidelity. The strain components calculated in the simulation were extracted from the element integration points on the surface that correspond to the painted surface in the tests. The strain profiles in the simulation, however, appear noisier than in the experiments. This could be due to the finer resolution achieved in the analysis since the element sizes used were significantly smaller than the strain gage length in the experiments. It could also be due to numerical noise in the simulations. Note that the predicted strain profiles show similar progression to those in the tests. The plots of ε_{rr} show maxima at $r/R \approx 0.6$ at the latest time plotted, similarly to what was observed in the experiments. In the case of $\varepsilon_{\theta\theta}$, local maxima are seen in the simulations in the vicinity of $r/R = 0.6$ for tests with $m \leq 420$ g, but in most cases a slightly higher spike appears at $r/R = 0$ at late times. In the case with $m = 500$ g a clear maximum in $\varepsilon_{\theta\theta}$ is seen at the center of the plate in both the experiment and the simulation. Also note the oscillatory nature of the radial strain profiles near the edge of the plate ($r/R = 1$, where bending dominates the deformation) in the simulations. These regions were not accessible for measurement in the experiments, but given the resolution of the DIC measurements, they could not have been determined anyway.

The numerical simulations produced the equivalent plastic strain plots shown in Figs. 40 to 43 (b). In all cases the maximum value of ε_e^p occurs at a location in the vicinity of $r/R = 0.6$. The case with a charge of 359 g shows a maximum of 0.16, whereas the other three show a maximum in the order of 0.18 to 0.19 at the time when tearing started in the experiments. This considerably underestimates the lower bound of the equivalent plastic strain values achieved in the bulge test described in Section 3, which were on the order of

0.3. Possible reasons for this discrepancy will be discussed in Section 7.

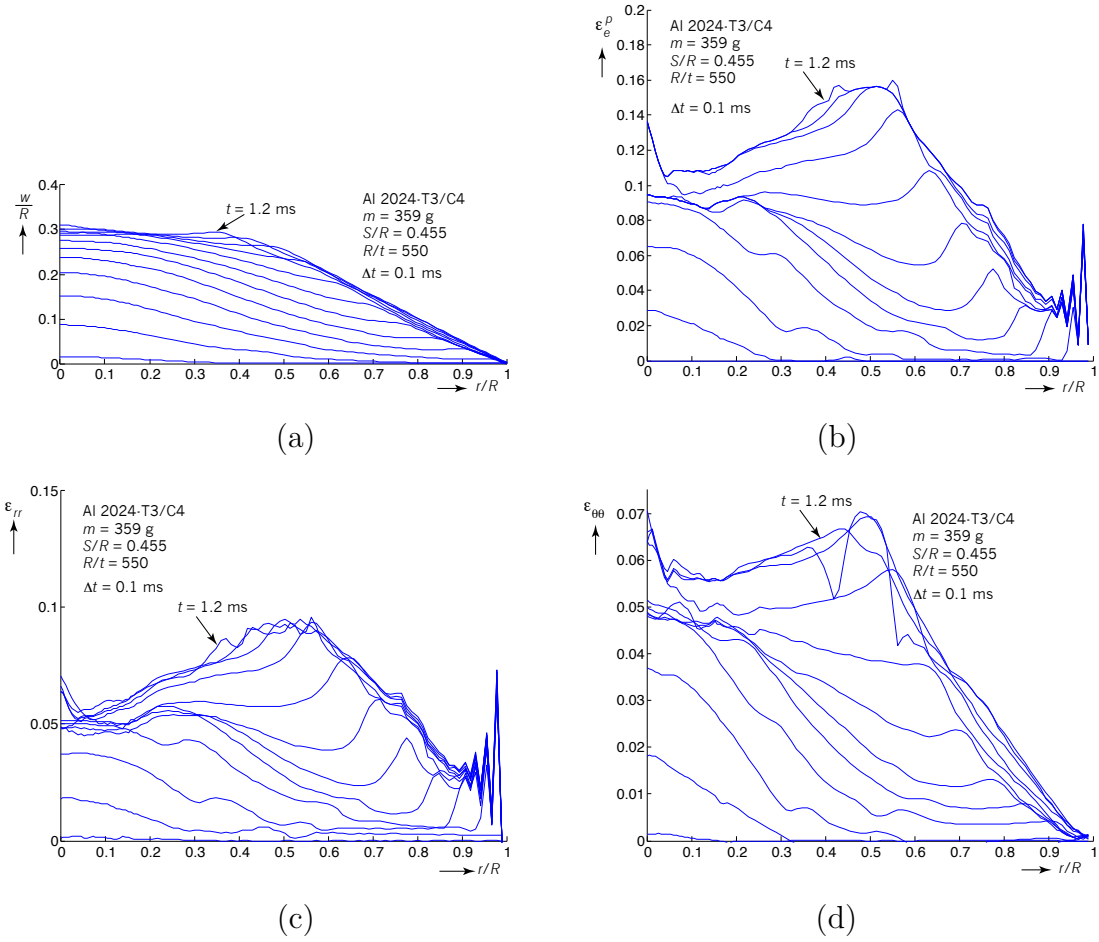

Figure 40. Calculated deflection and strain radial profiles for $m = 359$ g. (a) Plate profiles, (b) equivalent plastic strain, (c) radial strain and (d) circumferential strain.

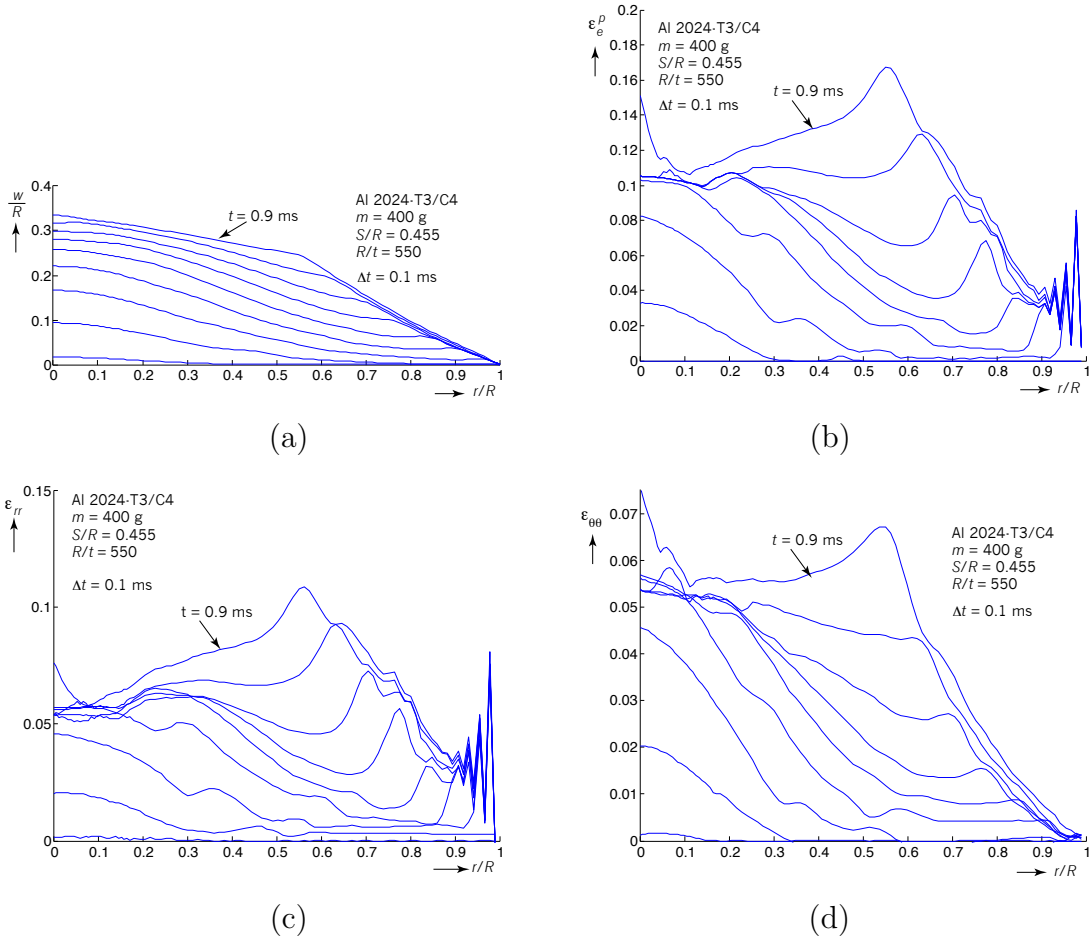

Figure 41. Calculated deflection and strain radial profiles for $m = 400$ g. (a) Plate profiles, (b) equivalent plastic strain, (c) radial strain and (d) circumferential strain.

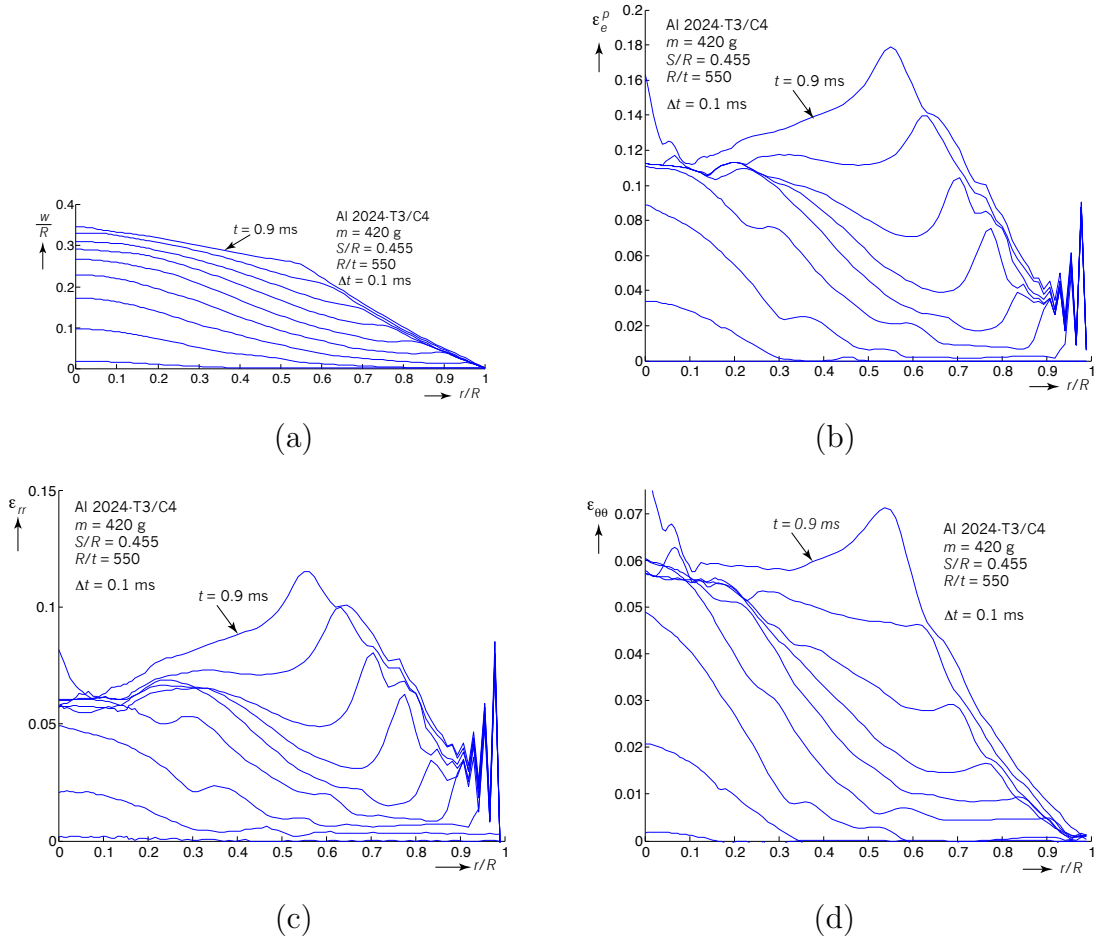

Figure 42. Calculated deflection and strain radial profiles for $m = 420$ g. (a) Plate profiles, (b) equivalent plastic strain, (c) radial strain and (d) circumferential strain.

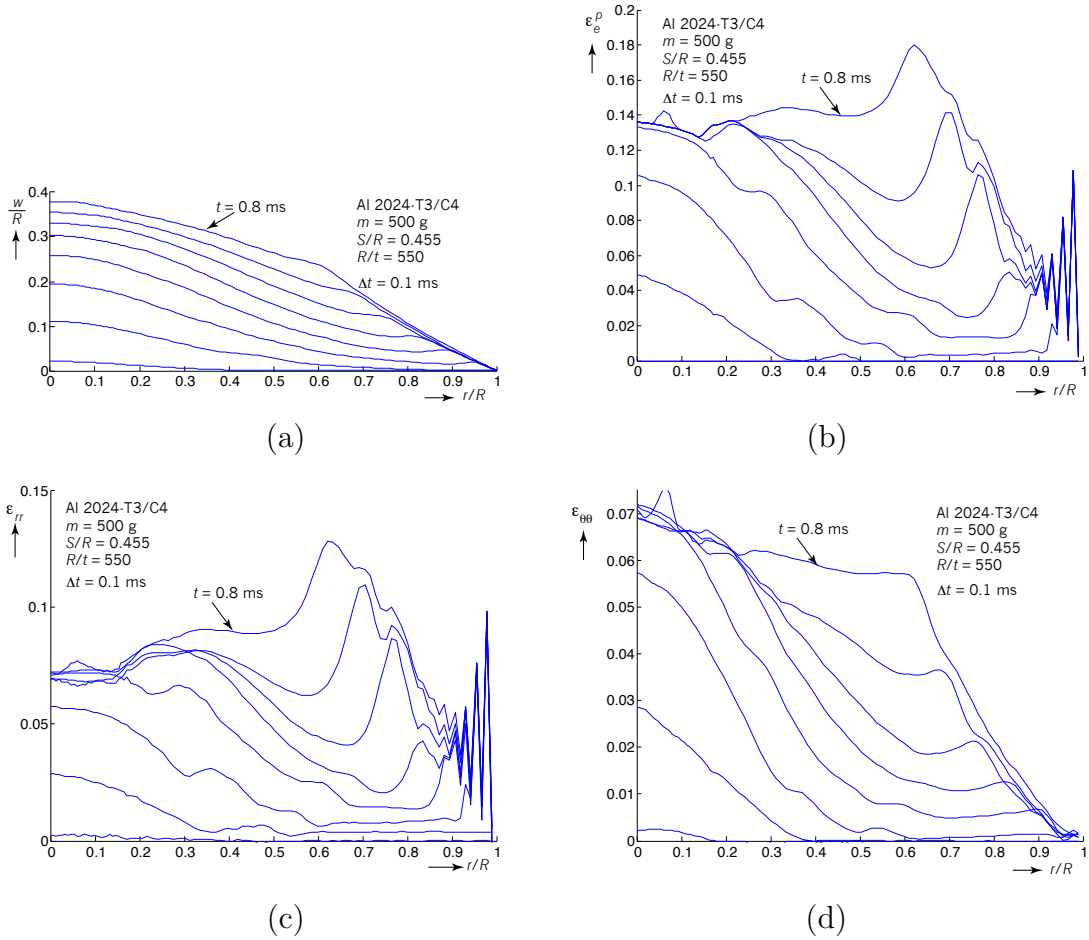

Figure 43. Calculated deflection and strain radial profiles for $m = 500$ g. (a) Plate profiles, (b) equivalent plastic strain, (c) radial strain and (d) circumferential strain.

7 Summary and Conclusions

In this work we addressed the response and failure of fully clamped, circular 2024-T3 aluminum alloy thin plates subjected to blast loading by nearby detonation of C4 spheres via experiments and numerical simulations. The plates had diameter of 44 in. and thickness of 0.040 in. A few cases with thickness of 0.063 in. were also considered to see if some of the analysis recommendations presented applied in that case as well. The standoff of the explosive charges was 10 in. The objective of the work was to conduct validation exercises on a fully (or two-way) coupled blast-structure interaction model.

High-speed, stereo DIC analysis was conducted for all the plates tested in order to estimate their deflections and strain as functions of position and time. Since the plate diameter was large, the strain calculations were made using a virtual strain gage with sides approximately 2.9 in. in length. Under these conditions the calculated values of the strain components just prior to failure were in the order of $\varepsilon_{rr} = 15\%$ and $\varepsilon_{\theta\theta} = 5\%$. The maximum radial strain occurred at a distance from the center of r/R between 0.6 to 0.8 and induced circumferential cracks to develop in that vicinity. The value of the charge at the threshold between no failure and failure of the plates was determined to be about 400 g from the experiments. Plates subjected to detonation by charges between 120 and 400 g suffered plastic deformations but did not fail. Their late-time responses were characterized by wrinkling.

Simulations conducted previously using an uncoupled blast/structure interaction model gave results that agreed well with experimental measurements of plate deflection but did not predict a failure mode that agreed with experiments. This was the principal motivation to undertake the current computational work using a fully coupled model. The model was implemented using the Sandia code Zapotec, which couples hydrodynamic blast predictions by CTH with a structural model in the finite element program Pronto3D.

The calculation of the blast in CTH used a JWL equation of state for the detonation products. The JWL parameters for C4 were taken from LNLL (2009), and used a programmed burn procedure to simulate detonation. The results obtained using the fully-coupled analysis indicated that the model underestimated the deflection of the plates by up to 20% for times greater than 0.5 ms when compared to experiment. Predictions of the deflection of the center of the plate prior to this time were actually in very good agreement with experiments. Search for the possible reasons for the discrepancy at later times pointed to insufficient loads on the plate. It was found that adding a constant 10 psi to the calculated blast pressures led to very good agreement between the measured and calculated plate deflections for all charges considered. This is in general agreement with the results presented by Alves et al (2012a), who postulated a long term energy release caused by the reaction of the detonation products with air (after-burn, see Alves et al, 2012b and Khul et al, 2000) that is not accounted for in the JWL model as the reason for the deficiency. Baudin and Serradeill (2010) also commented that the JWL model is commonly calibrated to be accurate for short times after the initiation of detonation. Therefore, the equation of state for longer times, after significant expansion of the products of detonation has occurred, is not accurate. Indeed, the cylinder expansion tests used to calibrate the JWL model look at the expansion rate of copper cylin-

ders that contain the explosive when the products of combustion have not expanded to the degree that is applicable for detonations in air. While we are not in a position to determine the physical reasons for the pressure deficit that is attributed to the detonation model, we recognize that the magnitude of the plate deflection is sensitive to relatively low-amplitude pressure fields late in time. It is also unreasonable to expect that a JWL model calibrated using cylinder tests and that neglects interaction with air to predict residual pressures that could be acting on the plate once the main pressure pulse has abated.

On the structural side, issues related to the behavior of the plate material remain the main sources of uncertainty when plate failure is considered. It has been shown that uniaxial tests of thin sheet material can be affected by local tensile instabilities. These lead to failure at relatively low strain values when measured over the length of the specimen test sections. Bulge tests, which subject the thin sheet material to biaxial loading yield equivalent strains that are much larger than those from uniaxial tests. If one is to consider predictions of failure of the plates, then it is important to determine the strain at failure of the material. Given that the strain at failure can be highly dependent on the state of stress, the bulge test has the advantage that it is under a biaxial state that is closer to that seen by the plates during blast loading than the uniaxial tension test. At this time, it is important to note that many papers in the literature such as Ghahremaninezhad and Ravi-Chandar (2012, 2013) and Haltom et al (2013) have indicated that the strains measured within the localization regions where tearing occurs are highly dependent on the size of the gage used to conduct the measurements. Smaller gage lengths give higher values of strain. This helps us provide a hypothesis for the paradox pointed out in the discussion of the results where it was noted that while the strains at failure seen in the bulge test were larger than 30%, the strains at failure measured in the blast loaded plates were in the vicinity of 18%. The hypothesis for this discrepancy is that the strains reported in the bulge tests were obtained by averaging the deformation over regions that were much smaller than those used in the blast loaded plates.

Looking at the numerical predictions, the local radial strains in the vicinity of the failure region at the time when failure occurred in the tests are even smaller than measured in the tests. This was so even though the element size was much smaller than the DIC strain gage length. We also note that the calculated deflections along the radius of the plate are about the same as seen experimentally. This brings another paradox: why are the strains at the time of failure in the simulation significantly smaller than the values achieved in the bulge test? Note that the question hinges on the applicability of the assumption that material failure occurs when the equivalent plastic strain reaches a critical value. Given that plates in the bulge test and in the blast test achieve biaxial tensile states, one could expect that they are reasonably close so that the equivalent plastic strain at failure would be comparable in both cases.

To partially address the question, we point out that it has been consistently reported in the literature that a von-Mises yield surface, as was used here, does not fit aluminum alloys as well as non-quadratic yield surfaces such as those proposed by Barlat et al (2005). Analyses that employ these yield functions have been shown to provide more accurate predictions

of deformation and localization in problems that involve aluminum alloys (Giagmouris et al, 2010). It has been observed that predictions using the von-Mises yield surface tend to underestimate the strain magnitudes in comparison with the non-quadratic surfaces, especially in problems that involve localization and failure. It is then possible that our analysis is deficient in this respect. Furthermore, recall that the models used in this work used shell elements to discretize the plate and are likely not well-suited to capture thinning localization events that are suspected to precede tearing of the plates.

Another possibility for this paradox that was not modeled in the present work concerns the strain-rate dependency of the material. Specifically, the question is whether failure can occur at much reduced strain levels when the strain rates are in the order of hundreds as in the blast tests instead of the very slow rates used in the material tests. Available strain rate sensitivity data of the failure strains of Al 2024-T3 (Kay, 2003) indicate that it is unlikely that the strain at failure would be reduced to the point suggested by the results of the simulations. It is more likely that the paradox introduced above has to do with a combination of the finite element discretization, through the type and size of the elements used, and the material model through the shape of the yield surface.

The next issue that needs to be addressed is the following: what can be done to increase confidence in failure calculations under scenarios similar to the one considered here? We note that in many instances engineers are unlikely to have the time and resources to investigate all aspects of a problem thoroughly. To further complicate matters, our knowledge in the topic of ductile failure remains deficient, and complex problems such as the one treated here make this clearly apparent. Given this state of affairs, it seems prudent that at least one calibration experiment that uses the actual structure and loading of interest be conducted to calibrate the failure model. If this is not possible, then at least a very close surrogate should be used. For example, given that the measured strain values at failure were comparable between all plates, and that the same can be said of the simulation results, it is likely that one test could have been used to establish the strains in the model at failure. That information could have subsequently been used to predict the failure of the others and to also estimate the explosive mass at the tearing threshold.

Clearly, complex multi-physics problems such as the one considered here must be investigated from combined experimental and analytical points of view if one is to have some reasonable degree of confidence in numerical predictions. In the present case, deficiencies and lack of knowledge in both the detonation model and the material model contributed to increase the uncertainty in the results. Without at least one experiment involving tearing, it would be impossible to determine the explosive mass threshold for failure of the plates. On a positive note, the evidence presented indicates that the fully coupled model predicted strain distributions that were at least qualitatively closer to the measurements in the experiments than those predicted by the uncoupled approach. They showed the highest values of equivalent plastic strain in the vicinity of the locations where tearing started in the specimens.

References

Adamson, D. 1878. On the Mechanical and Other Properties of Iron and Mild Steel *Journal of the Iron and Steel Institute*, **14**, pp. 383–403.

Alves, S., Kuhl, A., Najjar, F., Tringe, J., McMichael, L. and Glascoe, L. 2012a. Building and Efficient Model for Afterburn Energy Release, LLNL-PROC-528333, Lawrence Livermore National Laboratory. Submitted to the 82nd Shock and Vibration Symposium.

Alves, S., Minkoff, S., Glascoe, L. and McMichael., L. 2012b. Modeling of Bare Circular Plate Blast Experiments, NEXESS Center Report 2012-1035, Lawrence Livermore National Laboratories.

Ansys, 2011. Explicit Dynamics Brochure. www.ansys.com.

Attaway, S.W., Brown, K.H., Mello, F.J., Heinstein, M.W., Swegle, J.A., Ratner, J.A. and Zadoks, R.I., 2000. PRONTO3D User's Instructions: A Transient Dynamic Code for Nonlinear Structural Analysis. Sandia Report SAND98-1361, Sandia National Laboratories.

Balden, V.H. and Nurick, G.N. 2005. Numerical Simulation of the Post-Failure Motion of Steel Plates Subjected to Blast Loading, *International Journal of Impact Engineering*, **32**, pp. 14–34.

Barlat, F., Eretz, H., Yoon, J.W., Karabin, M.E., Brem, J.C. and Dick, R.E., 2005. Linear Transformation-Based Anisotropic Yield Functions, *International Journal of Plasticity*, **21**, pp. 1009–1039.

Baudin, G. and Serradeill, R. 2010. Review of Jones-Wilkins-Lee Equation of State, *EPJ Web of Conferences* DOI: 10.1051/epjconf/20101000021.

Bessette, G.C., Prentice, J.K., Bell, R.L., Vaughan, C.T. and Cole, R.A. 2003. Zapotec: A Coupled Eulerian-Lagrangian Computer Code, Methodology and User Manual, Version 2.67. Sandia Report SAND2003-3097, Sandial National Laboratories.

Blazynski, T.Z., Editor. 1983. Explosive Welding, Forming and Compaction, Applied Science Publishers Ltd. Essex, England.

Bodner, S.R. and Symonds, P.S. 1979. Experiments on Viscoplastic Response of Circular Plates to Impulsive Loading, *Journal of the Mechanics and Physics of Solids*, **27**, pp. 91–113.

Carroll, S.K., Drake, R.R., Hensinger, D.M., Luchini, C.B., Petney, S.V., Robbins, J., Robinson, A.C., Summers, R.M., Voth, T.E., Wong, M.K., Brunner, T.A., Garasi, C.J., Haill, T.A. and Mehlhorn, T.A. 2004. ALEGRA: Version 4.6. Sandia Report SAND2004-6541, Sandia National Laboratories.

Cloete, T.J., Nurick, G.N. and Palmer, R.N. 2005. The Deformation and Shear Failure of Peripherally Clamped Centrally Supported Blast Loaded Circular Plates, *International*

Journal of Impact Engineering, **32**, pp. 92–117.

Corona, E. and Reedlunn, B. 2013. A review of macroscopic ductile failure criteria, Sandia Report SAND2013-7989, Sandia National Laboratories.

Cowperthwaite, W. and Zwisler, W.H. 1973. TIGER Computer Program Documentation. SRI Publication No. Z106, Stanford Research Institute.

Crawford, D.A., Brundage, A.L., Harstad, E.N., Ruggirello, K., Schmitt, R.G., Schumacher, S.C. and Simmons, J.S. 2013. CTH User's Manual and Input Instructions, Version 10.3, Sandia National Laboratories.

Dassault Systemes Simulia, 2014. Abaqus 6.14 Analysis User's Guide. Providence RI.

Duffey, T.A. 1967. The Large Deflection Dynamic Response of Clamped Circular Plates Subjected to Explosive Loading, Report SC-RR-67-532, Sandia National Laboratories.

Duffey, T.A. and Key, S.W. 1968. Experimental-Theoretical Correlations of Impulsively Loaded Clamped Circular Plates, Report SC-RR-68-210, Sandia National Laboratories.

Farhat, C, Wang, K.G., Main, A., Kyriakides, S., Lee, L.-H., Ravi-Chandar, K. and Belytschko, T. 2013. Dynamic Implosion of Underwater Cylindrical Shells: Experiments and Computations, *International Journal of Solids and Structures*, **50**, pp. 2943–2961.

Florence, A.L. 1966. Clamped Circular Rigid-Plastic Plates Under Centeral Blsast Loading, *International Journal of Solids and Structures*, **2**, pp. 319–335.

Florence, A.L. 1979. Response of Circular Plates to Central Pulse Loading, *International Journal of Solids and Structures*, **13**, pp. 1091–1102.

Gharababaei, H., Darvizeh, A. and Darvizeh, M. 2010. Analytical and Experimental Studies for Deformation of Circular Plates Subjected to Blast Loading, *Journal of Mechanical Science and Technology*, **24**, pp. 1855–1864.

Giagmourris, T., Kyriakides, S., Korkolis, Y.P. and Lee, L.-H., 2010. On the Localization and Failure in Aluminum Shells Due to Crushing Induced Bending and Tension, *International Journal of Solids and Structures*,**47**, pp. 2680–2692.

Gupta, N.K. and Nagesh. 2007. Deformation and Tearing of Circular Plates with Varying Support Conditions Under Uniform Impulsive Loads, *International Journal of Impact Engineering*, **34**, pp. 42–59.

Hertel, E.S. and Kerley, G.I. 1998. CTH Reference Manual: The Equation of State Package. Sandia Report SAND98-0947, Sandia National Laboratories.

Hodowany, J., Ravichandran, G., Rosakis, A.J. and Rosakis, P. 2000. Parititon of Plastic Work into Heat and Stored Energy in Metals, *Experimental Mechanics*, **40**, pp. 113–123.

Hoffman, A.J. 1955. The Plastic Response of Circular Plates to Air Blast, Master of Me-

chanical Engineering Thesis, University of Delaware, 1955.

Hudson, G.E. 1951. A Theory of the Dynamic Plastic Deformation of a Thin Diaphragm, *Journal of Applied Physics*, **22**, pp. 1–11.

Jacob, N., Chung Kim Yuen, S., Nurcik, G.N., Bonorchis, D., Desai, S.A. and Tait, D. 2004. Scaling Aspects of Quadrangular Plates Subjected to Localised Blast Loads—Experiments and Predictions, *International Journal of Impact Engineering*, **30**, pp. 1179–1208.

Jacob, N., Nurick, G.N. and Langdon, G.S. 2007. The Effect of Stand-off Distance on the Failure of Fully Clamped Circular Mild Steel Plates Subjected to Blast Loads, *Engineering Structures*, **29**, pp. 2723–2736.

Kalpakjian,S. 1995. Manufacturing Engineering and Technology, Addison-Wesley Publishing Company, pp. 487–488.

Kay, G. 2003. Failure Modeling of Titanium 6Al-4V and Aluminum 2024-T3 with the Johnson-Cook Material Model. Report No. DOT/FAA/AR-03/57. U.S. Department of Transportation, Federal Aviation Administration.

Krajcinovic, D. 1972a. Clamped Circular Rigid-Plastic Plates Subjected to Central Blast Loading, *Computer & Structures*, **2**, pp. 487–496.

Kracinovic, D. 1972b. Dynamic Analysis of Clamped Plastic Circular Plates, *International Journal of Mechanical Sciences*, **14**, pp. 225–234.

Kuhl, A.L., Oppenheim, A.K., Ferguson, R.E., Reichenbach, H. and Neuwald, P. 2000. Effects of Confinement on Combustion of TNT Explosion Products in Air, Preprint UCRL-JC-137418, Lawrence Livermore National Laboratory. Submitted to the 28th International Symposium on Combustion.

Kyriakides, S. and Mersch, J.P. 2013. Hydraulic Bulge Test for Thin Sheets, report to Sandia National Laboratories.

Kyriakides, S. 2014. Personal communication.

LLNL. 2009. LLNL Explosive Reference Guide, Lawrence Livermore National Laboratory. Online limited access website.

Langdon, G.S. and Schleyer, G.K. 2003. Inelastic Deformation and Failure of Clamped Aluminum Plates Under Pulse Pressure Loading, *International Journal of Impact Engineering*, **28**, pp. 1107–1127.

Larsen, M., Haulenbeek, K., Corona, E., Rath, J., Reu, P., Gruda, J., Phelan, J. and Gwinn, K. 2012. Assessment of Mass Factors Based on Structural Damage Equivalence of Thin Circular Plates, Nexess Center Report 2012-0104, Sandia National Laboratories.

Lee, E.L., Horning, H.C. and Kury, J.W. 1968. Adiabatic Expansion of High Explosive Detonation Products. Report UCRL-50422, Lawrence Radiation Laboratory.

Lesuer, D.R. 2000. Experimental Investigations of Material Models for Ti-6Al-4V Titanium and 2024-T3 Aluminum. Report No. DOT/FAA/AR-00/25. U.S. Department of Transportation, Federal Aviation Administration.

Mersch, J.P. 2013. On the Hydraulic Bulge Testing of Thin Sheets, Master of Science in Engineering Thesis, The University of Texas at Austin.

Neuberger, A., Peles, S. and Rittel, D. 2007 Scaling the Response of Circular Plates Subjected to Large and Close-Range Spherical Explosions. Part I: Air-Blast Loading, *International Journal of Impact Engineering*, **34**, pp. 859–873.

Nichols III, A.L., Ed. 2011. User's Manual for ALE3D, an Arbitrary Lagrange/Eulerian 2D and 3D Code System, Volumes 1 and 2, Version 4.14.x, LLNL-SM-471671. Lawrence Livermore National Laboratory.

Nurick, G.N., Gelman, M.E. and Marshall, N.S. 1996. Tearing of Blast Loaded Plates with Clamped Boundary Conditions, *International Journal of Impact Engineering*, **18**, pp. 803–827.

Nurick, G.N. and Martin, J.B. 1989. Deformation of Thin Plates subjected to Impulsive Loading—A Review. Part I: Theoretical Considerations, *International Journal of Impact Engineering*, **8**, pp. 159–170.

Nurick, G.N. and Martin, J.B. 1989. Deformation of Thin Plates subjected to Impulsive Loading—A Review. Part II: Experimental Studies, *International Journal of Impact Engineering*, **8**, pp. 171-186.

Nurick, G.N. and Shave, G.C. 1996. The Deformation and Tearing of Thin Square Plates Subjected to Impulsive Loads—An Experimental Study, *International Journal of Impact Engineering*, **18**, pp. 99–116.

Pearson, J. 1983. Introduction to High-Energy-Rate Metalworking, in Explosive Welding, Forming and Compaction, Blazynski, T.Z. Editor, Applied Science Publishers Ltd. Essex, England.

Rajendran, R. and Narasimhan, K. 2001. Damage Prediction of Clamped Circular Plates Subjected to Contact Underwater Explosion, *International Journal of Impact Engineering*, **25**, pp. 373-386.

Ramajeyathilagam, K., Vendhan, C.P. and Bhujanga Rao, V. 2000. Non-linear Transient Dynamic Response of Rectangular Plates Under Shock Loading, *International Journal of Impact Engineering*, **24**, pp. 999-1015.

Rudrapatna, N.S., Vaziri, R. and Olson, M.D. 1999. Deformation and Failure of Blast-Loaded Square Plates, *International Journal of Impact Engineering*, **22**, pp. 449–467.

Safari, K.H., Zamani, J., Khalili, S.M.R. and Jalili, S. 2011. Experimental, Theoretical, and Numerical Studies on the Response of Square Plates Subjected to Blast Loading, *The*

Journal of Strain Analysis for Engineering Design, **46**, pp. 805–816.

Sierra Solid Mechanics Team. 2013. Sierra/Solid Mechanics 4.30 User's Guide: Addendum for Shock Capabilities, Sandia National Laboratories.

Sierra Solid Mechanics Team. 2014. Sierra/Solid Mechanics 4.34 User's Guide, Sandia National Laboratories.

Corona, E. and Reedlunn, B. 2013. A review of macroscopic ductile failure criteria, Sandia Report SAND2013-7989, Sandia National Laboratories.

Sutton, D.A., Orteu, J.J. and Schreier, H.W. 2009. Image Correlation for Shape, Motion and Deformation Measurements. Springer, New York.

Taylor, G.I. 1941. The Pressure and Impulse of Submarine Explosion Waves on Plates-The Scientific Papers of G.I. Taylor, Vol. III, pp. 287–303, Cambridge University Press.

Teeling-Smith, R.G. and Nurick, G.N. 1991. The Deformation and Tearing of Thin Circular Plates Subjected to Impulsive Loads, *International Journal of Impact Engineering*, **11**, pp. 77–91.

Tiwari, V., Sutton, M.A., McNeill, S.R., Xu, S., Deng, X., Fourney, W.L. and Bretall, D. 2009. Application of 3D Image Correlation for Full-Field Transient Plate Deformation Measurements During Blast Loading, *International Journal of Impact Engineering*, **36**, pp. 862–874.

Veldman R.L., Ari-Gur, J., Clum, C., DeYoung, A. and Folkert, J. 2006. Effects of Pre-pressurization on Blast Response of Clamped Aluminum Plates, *International Journal of Impact Engineering*, **32**, pp. 1678–1695.

Veldman, R.L., Ari-Gur, J. and Clum, C. 2008. Response of Pre-Pressurized Reinforced Plates Under Blast Loading, *International Journal of Impact Engineering*, **35**, pp. 240–250.

Wang, A.J. and Hopkins, H.G. 1954. On the Plastic Deformation of Built-in Circular Plates Under Impulsive Load, *Journal of the Mechanics and Physics of Solids*, textbf8, pp. 22–37.

Wierzbicki, T. and Nurick, G.N. 1996. Large Deformation of Thin Plates Under Localized Impulsive Loading, *International Journal of Impact Engineering*, **18**, pp. 899–918.

Witmer, E.A., Balmer, H.A., Leech, J.W. and Pian, T.H.H. 1963. Large Dynamic Deformations of Beams, Rings, Plates and Shells, *AIAA Journal*, **1**, pp. 1848–1857.

A Uncertainty in Mean Axisymmetric Displacement and Strain Measurements

The calculations of displacement and strain from the DIC data contain several inherent averaging schemes that were discussed in Section 2.2. The objective of this Appendix is to present some examples that show some of the effects of this averaging.

A.1 Circumferential averaging

Figure A.1 (a) shows displacement profiles for $m = 359$ g calculated by averaging the measured displacements in the circumferential direction. The solid lines represent the average values at five times similar to those plotted throughout the presentation of the experimental results. The dashed lines represent plus/minus two standard deviations from the mean. Clearly, the spread shown grows somewhat with time but is always small compared to the mean displacements. Note that even at $t = 2.2$ ms, which is well after the specimen had wrinkled, the bounds are relatively tight about the mean.

The radial and circumferential strain components, shown in Figs. A.1(b) and (c) respectively, show wider 2-standard-deviation bands. This is as expected since the strain components depend on the gradient of the displacement components and are inherently noisier. Still, the spread seems reasonable compared to the mean values in all but one case. Whereas the measured radial strain does not show the effects of wrinkling in the 2.2 ms traces, the circumferential strain does show them very clearly. Note that the two-standard-deviation bands are much larger for the 2.2 ms trace than for any of the others. Clearly the development of wrinkles aligned in the radial direction causes large fluctuations of the circumferential strain on the surface of the specimen.

A.2 Effect of Virtual Strain Gage Length

As was mentioned in the body of the report, the measurement of strain requires at least a region that contains 5×5 points where the displacement components have been measured, thus giving a 'strain gage length' of 13 pixels, and the reported values are in some sense averaged over a region with corresponding dimensions. Whereas it was not practical, and perhaps not even possible, to determine the strains measured with smaller virtual gage lengths, it is possible to consider longer lengths to see the effect. Figure A.2 shows examples of radial and circumferential strains calculated with two virtual gage lengths, 13 and 25 pixels, equivalent to 2.9 and 5.5 in. The results are as expected, with the longer virtual gage length giving smoother strain distributions that underestimate the strain gradients. Clearly, even the 13 pixel virtual gage is too large to capture the strain localizations that give rise to tearing of the specimens.

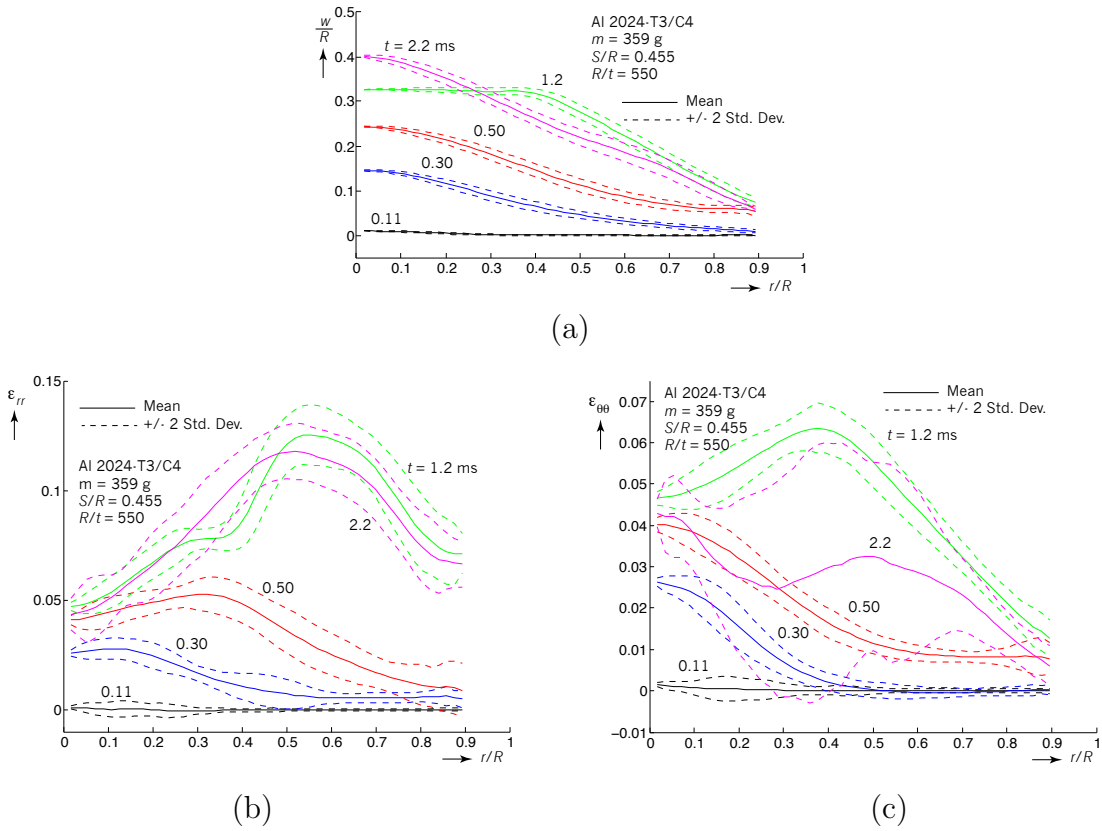

Figure A.1. Plots showing ±2 standard deviations from the means calculated in the axisymmetric analysis of the plate response for $m = 359$ g. (a) Normal displacement, (b) radial strain and (c) circumferential strain.

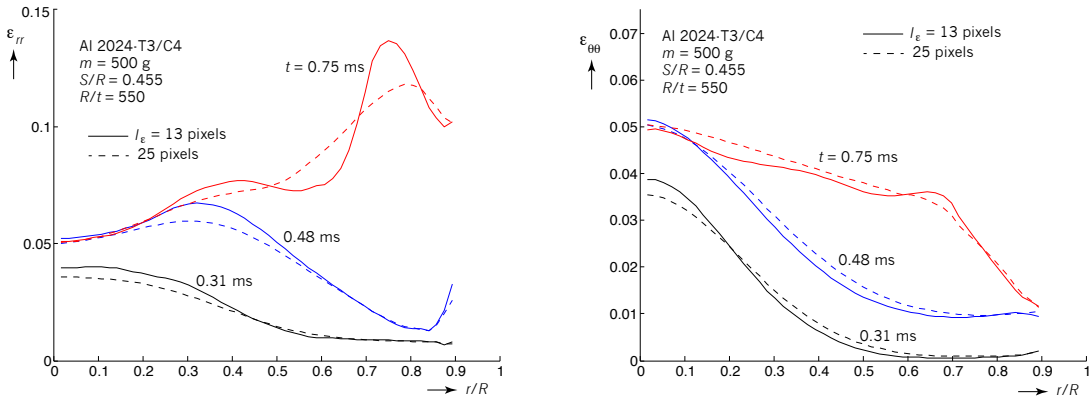

Figure A.2. Effect of the virtual strain gage used in the calculation of the strain from the stereo DIC analysis. The plots compare the results presented in the rest of the report with a virtual gage length of 2.9 in to those obtained with a virtual gage length 2.2 times as long. (a) Radial strain and (b) circumferential strain.

B Calculation of Von-Mises Equivalent Stress and Strain in the Bulge Test

The procedure used by Kyriakides and Mersch (2013) to calculate the von-Mises equivalent stress-strain curve of the plate material using the bulge test was given as follows:

1. The apex of the bulge is under equibiaxial tension. The DIC analysis is used to evaluate the logarithmic strain components e_1 and e_2 at the apex and the local radius of curvature R.

2. The local stresses are $\sigma_1 = \sigma_2 = PR/2t$, and the equivalent von-Mises stress is $\sigma_e = PR/2t$, where P is the measured pressure and t is the current sheet thickness.

3. Once the stress and strain components are known, the plastic strain components e_1^p and e_2^p can be calculated by subtracting the elastic strain components calculated using Hooke's law. The through-thickness plastic strain is evaluated by assuming plastic incompressibility, $e_3^p = -(e_1^p + e_2^p)$. This condition also allows to iteratively determine the value of t used in the stress calculations.

4. The equivalent plastic strain is then given by

$$e_e^p = \left[\frac{2}{3}\left(e_1^{p2} + e_2^{p2} + e_3^{p2}\right)\right]^{1/2}.$$

   If the material is taken to be plastically isotropic, $e_1^p = e_2^p$ and $e_e^p = 2e_1^p$.

DISTRIBUTION:

1 S. Alves, Lawrence Livermore National Laboratory

1 MS 0421 J. Gruda, 00158
1 MS 0557 K. Haulenbeek, 01558
1 MS 0757 K. Metzinger, 06626
1 MS 0782 J. Phelan, 06633
1 MS 0815 J. Johannes, 01500
1 MS 0828 T. Durbin, 01512
1 MS 0828 P. Reu, 01512
1 MS 0840 J. Redmond, 01550
1 MS 0840 E. Corona, 01554
1 MS 0840 H. Fang, 01554
1 MS 0840 K. Gwinn, 01554
1 MS 0840 B. Reedlunn, 01554
1 MS 0840 W. Scherzinger, 1554
1 MS 0840 S. Attaway, 01555
1 MS 0840 M. Bailey, 01555
1 MS 0840 J. Pott, 01555
1 MS 0840 J. Rath, 01555
1 MS 1185 A. Gullerud, 05417
1 MS 1185 E. Hertel, 05417
1 MS 1231 D. Joe, 05439
1 MS 1454 M. Cooper, 02554
1 MS 9042 W.-Y. Lu, 08256
1 MS 0899 Technical Library, 9536 (electronic copy)

Sandia National Laboratories